FINAL REPORT
NASA Project NAG 5-2589
July 1, 1994 - August 31, 1995

Observational and Numerical Studies of Extreme Frontal Scale Contraction

prepared for the

Science Division
Office of Mission to Planet Earth
NASA Headquarters
Washington, D. C. 20546

Attention: Dr. Ramesh Kakar, Program Manager

by

Dr. Steven E. Koch

Department of Marine, Earth, and Atmospheric Sciences
North Carolina State University
Box 8208
Raleigh, NC 27695-8208

October 1995

FINAL REPORT
NASA Project NAG 5-2589
July 1, 1994 - August 31, 1995

Observational and Numerical Studies of Extreme Frontal Scale Contraction

prepared for the

Science Division
Office of Mission to Planet Earth
NASA Headquarters
Washington, D. C. 20546

Attention: Dr. Ramesh Kakar, Program Manager

by

Dr. Steven E. Koch

Department of Marine, Earth, and Atmospheric Sciences
North Carolina State University
Box 8208
Raleigh, NC 27695-8208

October 1995

Table of Contents

Acknowledgements

I would like to thank Dr. Ramesh Kakar at NASA Headquarters for his generous financial support of the research conducted under this grant, and to Dr. Rober Adler at NASA/Goddard Space Flight Center for his encouragement and support of this project. The foundations for part of this effort were laid while I was still at Goddard. Thus, I would like to express my appreciation to the following persons who contributed to the success of this project during those years: Mr. Jefferey McQueen, who performed many of the Eady wave simulations; Dr. Mohan Karyampudi, who assisted in the interpretation of the model output and provided the Blackadar boundary layer code used in the MASS model; the GEMPAK programming staff at Goddard, including in particular Ms. Mary desJardins and Mr. James Whistler; and Mr. Harold Pierce for his assistance with the satellite - GEMPAK interface used in displaying the COPS-91 data. In addition, I wish to express my gratitude to Mr. Wallace Clark of NOAA's Aeronomy Lab for his diligent work with the analysis of the Wind Profiler data and to Dr. Edward Brandes of NCAR for assistance with collecting some of the Doppler radar and other remote sensing data from COPS-91. The assistance provided by Dr. Chaing Chen at Goddard in using his model was of immeasurable benefit to this project. Stimulating discussions with Dr. F. Martin Ralph at NOAA/ERL/ETL and Dr. Yuh-Lang Lin at NCSU contributed significantly to the gravity current modeling study. The gravity current simulations were performed on the CRAY Y-MP at the North Carolina Supercomputing Center. Part of the calculations were executed and displayed using the IBM-funded FOAM^{V} facilities at North Carolina State University.

Executive Summary

The general objective of this effort is to increase understanding of how frontal scale contraction processes may create and sustain intense mesoscale precipitation along intensifying cold fronts. The five-part project (an expansion of the originally proposed two-part project) employed conventional meteorological data, special mesoscale data, remote sensing measurements, and various numerical models. **First**, an idealized hydrostatic modeling study of the scale contraction effects of differential cloud cover on low-level frontal structure and dynamics was completed and published in a peer-reviewed journal. The **second** objective was to complete and publish the results from a three-dimensional numerical model simulation of a cold front in which differential sensible heating related to cloud coverage patterns was apparently crucial in the formation of a severe frontal squall line. The **third** objective was to use a nonhydrostatic model to examine the nonlinear interactions between the transverse circulation arising from inhomogeneous cloud cover, the adiabatic frontal circulation related to semi-geostrophic forcing, and diabatic effects related to precipitation processes, in the development of a density current-like microstructure at the leading edge of cold fronts. Although the development of a frontal model that could be used to initialize such a primitive equation model was begun, we decided to focus our efforts instead on a project that could be successfully completed in this short time, due to the lack of prospects for continued NASA funding beyond this first year (our proposal was not accepted for future funding). Thus, a **fourth** task was added, which was to use the nonhydrostatic model to test tentative hypotheses developed from the most detailed observations ever obtained on a density current (primarily sodar and wind profiler data). These simulations were successfully completed, the findings were reported at a scientific conference, and the results have recently been submitted to a peer-reviewed journal. The **fifth** objective was to complete the analysis of data collected during the Cooperative Oklahoma Profiler Studies (COPS-91) field project, which was supported by NASA. The analysis of the mesoscale surface and sounding data, Doppler radar imagery, and other remote sensing data from multi-frequency wind profiler, microwave radiometer, and the Radio Acoustic Sounding System has been completed. This study is a unique investigation of processes that caused the contraction of a cold front to a microscale zone exhibiting an undular bore-like structure. Results were reported at a scientific conference and are being prepared for publication. In summary, considerable progress has been achieved under NASA funding in furthering our understanding of frontal scale contraction and density current - gravity wave interaction processes, and in utilizing models and remotely sensed data in such studies.

1. Overview

Accurate prediction of precipitation patterns and amounts requires a much better understanding of the structural evolution and dynamics of cyclones, jet-front systems, embedded mesoscale circulation systems, and the mesoscale and microscale physical processes at work. Forcing mechanisms for mesoscale precipitation systems involve highly interacting, nonlinear processes that cover a broad range of atmospheric scales. The research discussed in this report deals with scale-interactive processes that cause the contraction of lower tropospheric fronts from broad zones to microscale structures capable of directly forcing strong frontal convection. Many of these squall line systems develop into large, long-lived mesoscale convective systems that can produce copious precipitation, extensive cirrus cloud systems, severe weather, and sometimes even new jet streaks due to the response of the momentum to large upward fluxes of heat and mass in the convection. Thus, these systems have profound effects upon the regional water and energy budgets.

The research conducted herein is concerned with understanding processes that produce (1) the "line convection/clear zone" (LC/CZ) phenomenon shown by Koch (1984) and Dorian et al. (1988) to be the precursor to the formation of some frontal squall lines, and (2) the "narrow cold-frontal rainband" (NCFR), a phenomenon that appears to have similarity to a density current due to diabatic effects related to precipitation processes (Carbone 1982; Parsons et al. 1987; Moncrieff 1989; Koch and Kocin 1991). The necessity of diabatic cooling for creating such structures is unresolved. Moreover, it is not clear whether any dynamical distinctions exist between these various shallow frontal convective line phenomena. Special datasets recently collected from a multi-scale field program, supported in part by NASA, and in which the P. I. participated, as well as primitive equation numerical models containing comprehensive physics, are employed in the investigation to further the basic understanding of frontal scale contraction processes. This final report summarizes the findings from a five-stage investigation of frontal scale contraction involving:

(1) an idealized hydrostatic modeling study of the effects of differential sensible on frontal structure and dynamics, in which the inhomogeneous heating arises from cross-frontal differences in cloud amount;

(2) a three-dimensional simulation of an observed LC/CZ case, in which a satellite-based moisture analysis scheme is developed and used to represent the mesoscale cloud field;

(3) a nonhydrostatic modeling study of the interactions between the transverse frontal circulations arising from cloud radiative effects, and adiabatic and diabatic processes;

(4) a nonhydrostatic modeling study of a density current and associated gravity waves that was observed in great detail by Doppler wind profiler and sodar systems; and

(5) an analysis of conventional, mesoscale, and remote sensing data collected on a scale-contracted front during a field project in Oklahoma.

2. Task 1: Model Study of the Effects of Clouds on Frontal Scale Contraction

2.1 Background on frontal scale contraction processes

The relative roles played by adiabatic frontogenesis, friction, and diabatic effects in frontal "scale contraction" are not well understood. Two-dimensional primitive equation models of frontogenesis have indicated that extreme scale contraction leading to a density current-like feature at the surface front ("frontal collapse") can develop *in the absence of precipitation* when sensible heating occurs ahead of an idealized front. This development appears to be caused by the acceleration of cold air under the influence of the pressure gradient that has been enhanced by the heating (Reeder 1986; Garratt and Physick 1986; Garratt 1988; Howells and Kuo 1988). Likewise, analysis of observations has shown that a narrow (< 5 km wide) band of shallow but vigorous, essentially two-dimensional "line convection" can develop at nonprecipitating fronts, and is oftentimes accompanied by intense (1-5 m s^{-1}) updrafts within a microscale region resembling a density current (Berson 1958; Brundidge 1965; Koch 1984; Shapiro 1984; Young and Johnson 1984; Shapiro et al. 1985; Garratt 1988; Dorian et al. 1988). Fair agreement has been found between the observed frontal speed and the theoretical speed of propagation of steady density currents, but Smith and Reeder (1988) point out that there is considerable uncertainty in the choice of predictor parameter values, that frontal systems are often *unsteady*, and that observed airflow patterns often do not show the cold air being advected toward its leading edge by a "feeder flow" extending back to the source of the cold air. *A fundamental issue then is whether and how a density current balance can evolve in dry cold fronts.*

Semi-geostrophic (SG) theory provides a basis for understanding how frontogenesis is forced by geostrophic deformation in an adiabatic and inviscid atmosphere (e.g., Hoskins 1971; Hoskins and Bretherton 1972; Blumen 1980). The Hoskins-Bretherton finite-amplitude, nonlinear extension to the Eady (1949) linear baroclinic wave problem describes the frontogenetical effects of horizontal shear deformation acting upon the along-front temperature gradient $[(\partial v_g/\partial x)(\partial\theta/\partial y)]$. Implicit to this theory is the geostrophic momentum approximation, according to which the parcel acceleration is replaced by dV_g/dt, i.e., a balanced flow (small Rossby number) is assumed (Hoskins 1975). Although certain features predicted by SG theory are qualitatively similar to those seen in analyses of actual cold fronts, the theory contains major shortcomings. These include its inability to account for the existence of an intense, narrow updraft jet near the top of the planetary boundary layer (PBL) and differing PBL structures across the front. The secondary circulation predicted by SG theory is quite broad (the separation between the centers of rising and sinking motion being nearly 1000 km) and weak, unless the models are run out for longer than a few days. Other serious limitations of SG theory are that it implicitly assumes the time-scale over which the flow accelerates is large compared

to the inertial time-scale, and that the accompanying transverse circulation preserves cross-front thermal wind balance.

Largely for these reasons, modelers have attempted to introduce various physical processes not contained in SG theory, by using the SG solutions as initial conditions for 2D primitive equation models. For example, the inclusion of diffusion processes prevents infinite cross-frontal gradients from occurring as they do in SG analytical models (Williams 1974). Although a weak updraft jet develops when using simplified boundary layer treatments like the Ekman PBL and bulk-aerodynamic formulae (Blumen 1980), Keyser and Anthes (1982) show that the introduction of frictional and turbulent momentum fluxes in a high-resolution PBL is required to produce an acceptable updraft jet structure, PBL stability patterns across the front, and the vertical structure of the frictionally-induced ageostrophic inflow feeding the updraft jet. An updraft of 7 cm s^{-1} was attained after 84 h in their 40 km resolution hydrostatic model initialized with the Hoskins and Bretherton (1972) horizontal shear model (or "Eady wave" model) of frontogenesis. An identical updraft strength has appeared in simulations with the same model that included explicit precipitation processes (Hsie and Anthes 1984; Hsie et al. 1984; Knight and Hobbs 1988), using grid meshes of 5-40 km. Benard et al. (1992) employed a 5 km resolution *nonhydrostatic* model that was initialized with the Eady wave solutions. This model produced a narrow cold-frontal rainband associated with an updraft jet of 35 cm s^{-1} forced by the combined actions of condensational heating and PBL friction. However, the role of latent heating on frontogenesis at low levels was rather small.

By contrast, sensible heating can intensify the cross-frontal temperature gradient at low levels when the fluxes are strongest in the warm air ahead of the front (Pinkerton 1978). The basic dynamics of the thermally-forced circulation resulting from diurnal variation of temperature contrast across a front was elucidated by Sun and Ogura (1979). They showed that differential development of the mixed layer across the front (such as results from inhomogeneous cloud cover) drives a solenoidal circulation, whose location and intensity are rather sensitive to the direction of the background wind. Their model atmosphere was characterized by a cross-front geostrophic wind shear $(\partial u_g/\partial z)$ *without* frontogenetical forcing by geostrophic deformation. A concentrated updraft with a maximum intensity of 30 cm s^{-1} developed near the deepest part of the mixed layer, and a compensating downdraft appeared about 60 km behind the updraft in the inversion capping the shallower mixed layer in the cool air. Segal et al. (1986) showed in another *non-frontal* 2D study that the imposition of differential cloud cover can result in an updraft similar to that typifying sea-breezes. Segal et al. (1993) found that cloud shading in the cold air behind a front will enhance frontogenesis only if the shading is prolonged, the cloud cover is sufficiently overcast, and the ground moisture availability is low. In contrast to these studies, the thermal contrast across the front can be weakened when the strongest sensible heating effects occur behind the front, as demonstrated

in a simulation of an arctic front by Thompson and Burk (1991). Reeder (1986) made use of a zonal shear flow in thermal wind balance to study the change in structure of a shallow front as it passed from cool ocean waters to a heated land mass. This model produced an updraft jet of 24 cm s^{-1} at 1.2 km above the ground; the front also developed a density current-like "feeder flow" where the air moved faster than the front in a limited region at low levels behind the front (also see Physick 1988). The phenomenon seen in these simulations, however, was not a true steady density current, since it did not consist of a *continuous* feeder flow extending through the cold air.

The general purpose of the present study is to understand the effects of an overcast low cloud deck existing behind an idealized cold front as it passes over a land mass and experiences sensible heating in the warm air *ahead* of the front. A motivation for this study is the increasing observational evidence that cross-frontal cloud differences can intensify and contract the scale of continental cold fronts (Koch 1984; Dorian et al. 1988; Businger et al. 1991). Our experimental approach provides a systematic investigation of the sensitivity of the results to modeling approaches, the relative importance of static destabilization versus sensible heating gradients in producing the frontal updraft, and the role of density current dynamics and symmetric instability. For example, the sensitivity of the results to grid resolution has not been systematically tested previously. Also, the treatment of the PBL has varied from the bulk aerodynamic method with a simple convective adjustment scheme and neglect of momentum mixing effects (Reeder 1986), to a multi-level PBL model (Pinkerton 1978; Segal et al. 1986; Physick 1988; Segal et al. 1993), to the level 2.5 approximations of Mellor and Yamada (1974), to represent the turbulent transport of heat and momentum (Sun and Ogura 1979). The method of initializing the model has also varied widely. Physick (1988) relied on an unbalanced initial state, whereas the Sawyer (1956)-Eliassen (1962) equation was employed by Reeder (1986) to specify the frontal secondary circulation. In addition, some studies have arbitrarily *specified* either a sensible heating or a ground temperature contrast across the front, whereas others have more realistically allowed the fluxes and temperatures to evolve in response to imposed differences in solar irradiance through the surface energy balance. The study by Reeder (1986) was the only one to use budget equations to provide quantitative insight into the relative roles of various processes in the frontogenesis and updraft jet evolution. Our study also attempts to further examine the question of whether the leading edge of cold fronts under the influence of differential sensible heating can develop the local characteristics of a density current, which is a characteristic of thermally-forced circulations like the sea breeze (Simpson 1987).

2.2 Results of the modeling study

This numerical study investigated the frontogenetical and dynamical effects of a cross-frontal gradient in sensible heating resulting from the contrast between clear skies ahead of an idealized mid-latitude, dry, continental cold front and an overcast low cloud deck existing behind the front. A

systematic investigation of various numerical and dynamical factors that exerted an influence on modeled frontogenesis also was conducted. The results of this investigation have been published in Koch et al. (1995a).

A dry, hydrostatic, two-dimensional model was initialized with the Hoskins-Bretherton shear deformation model of frontogenesis. The simulated frontal structure and dynamics were sensitive to the type of parameterized boundary layer treatment. A bulk mixed-layer approach was found to be ill-suited to modeling frontogenesis in the presence of differential sensible heating, whereas the Blackadar multi-level PBL treatment produced realistic low-level jet and thermodynamic structures.

Introduction of uniform sensible heating (no clouds) produced a deep and narrow updraft jet (plume) at the leading edge of the modeled cold front, whose magnitude using a 10 km grid resolution was 16 cm s^{-1}. The strength of this updraft reached 22 cm s^{-1} in the differential sensible heating run, wherein completely overcast low cloud cover was specified west of the front, and clear skies to the east, resulting in a sensible heat flux of 450 W m^{-2} ahead of (and nearly zero behind) the front. Figure 1 compares the differences in frontal structure and strength between the adiabatic, inviscid model simulation (NOPHY) and the differential heating run including frictional effects (DIFHT). Notice that the front that contains the PBL heating/viscous physics is much more erect, contains a much deeper pre-frontal PBL and a stong updraft jet, displays a low-level alongfront jet on both sides of the front, and has a much stronger cross-front temperature gradient.

Drastic reduction of the along-front wind component v within the plume resulted in a strong ageostrophic component v_{ag} and associated maximum in the unbalanced ageostrophic vorticity. The latter feature acted as a significant source for ageostrophic cross-frontal wind divergence in mid-levels. The combination of this divergence with low-level convergence produced by frictional and diabatic effects explained the development of the frontal updraft jet. Although the greatest strengthening of the updraft in our simulations ensued from the introduction of sensible heating, rather than the introduction of an *inhomogeneity* in sensible heating, analysis indicates that the differences would be expected to be much larger at grid resolutions $\Delta x < 10$ km (requiring the use of a nonhydrostatic model), since sizable increase in frontal updraft intensity was realized *only* in the DIFHT case by decreasing the grid size.

Highly negative geostrophic potential vorticity developed within the updraft plume from the interaction of the low-level southerly geostrophic jet with the strong cross-frontal temperature gradient in the DIFHT case. Numerical experiments showed, curiously enough, that dry symmetric instability could not have played a significant role in driving the strong frontal updraft that characterized the secondary circulation. The simulated front in the DIFHT case displayed similarity

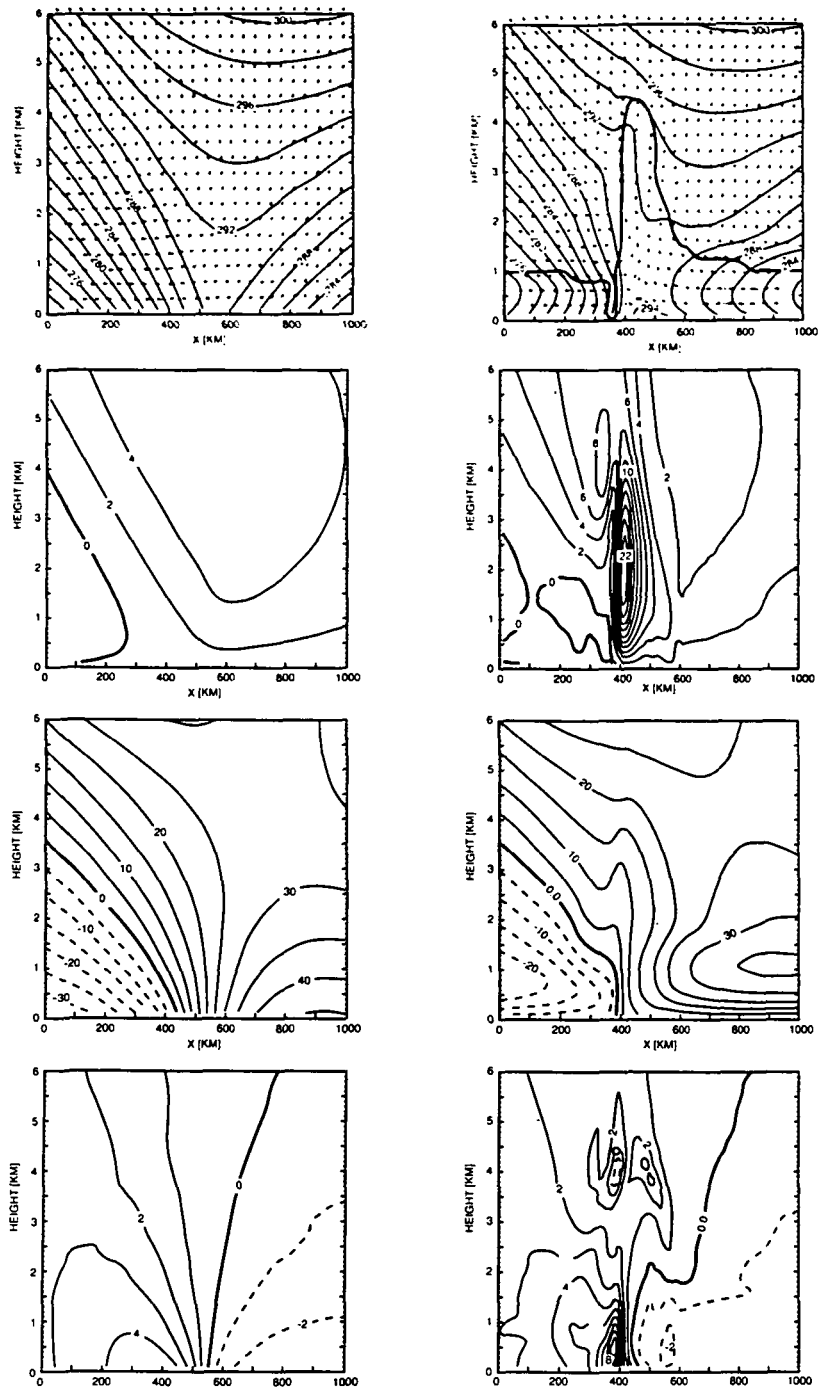

FIG. 1 Comparison of 10 km resolution model 7-h predictions for 2100 UTC from NOPHY (left) and DIFHT runs (right): (a, b) ageostrophic front-relative flow (vertical motions are exaggerated) and θ (contour interval 2K), with diagnosed PBL height h depicted by thick curve in panel b; (c, d) vertical velocity w (contour interval 2 cm s^{-1}); (e, f) along-front wind v (contour interval 5 m s^{-1}, with southerly (northerly) winds solid (dashed)); and (g, h) cross-front temperature gradient $\partial\theta/\partial x$ (contour interval of 1 K/100 km). Surface position of cold front for NOPHY case is at x = 550 km and at x = 400 km for DIFHT case. Only the lowest 6 km and the centermost 1000 km horizontal region of model domain are shown.

to a density current inasmuch as there was a "feeder flow" of post-frontal air at low levels extending back to the core of the cold air mass moving faster than the front, and the depth of this region was typical of atmospheric density currents (Fig. 2). Such an extensive feeder flow has not been seen in previous numerical models of frontogenesis. A similar (though weaker) region of positive front-relative flow existed in the homogeneous heating run. Since density currents are usually generated by fields of non-uniform diabatic heating (or cooling), this result may appear surprising. However, the strong front-relative flow in the homogeneous heating run developed as a consequence of the acceleration of the cross-frontal ageostrophic flow due to the effects of sensible heating.

Koch (1984) and Dorian et al. (1988) have reported cases of strong frontogenesis in which a frontal line convection developed in the presence of a strong cloud contrast across cold fronts. The findings from this idealized study of frontogenesis lend strong support to their hypothesis that a highly nonlinear interaction between the adiabatic, large-scale frontal circulation and the thermally-forced circulation produced by the cloud contrast produced the updraft that triggered the frontal squall lines. Those case studies were limited by their reliance upon synoptic surface and upper-air data, preventing any understanding of the three-dimensional mesoscale dynamics. Our model results show that frontogenesis was dominated by confluence forcing near the surface (Fig. 3c), lending support to the usefulness of surface frontogenesis diagnostics in observational studies lacking mesoscale data aloft. Diffluence-forced frontolysis in mid-levels appeared above the frontogenesis maximum in the model, a feature related to the updraft plume dynamics. Direct forcing of frontogenesis by the diabatic gradient term in the frontogenesis budget equation (Fig. 3f) produced only secondary effects; the primary frontogenetical forcing was due to an *indirect* effect of heating on enhancing the cross-front confluence (convergence). These terms are shown in the frontogenesis budget equation below

$$\underset{I}{\overline{\frac{d}{dt}\left(\frac{\partial\theta}{\partial x}\right)}^{x,t}} = \underset{II}{-\overline{\frac{\partial u}{\partial x}\frac{\partial\theta}{\partial x}}^{x,t}} \underset{III}{-\overline{\frac{\partial v}{\partial x}\frac{\partial\theta}{\partial y}}^{x,t}} \underset{IV}{-\overline{\frac{\partial\dot{\sigma}}{\partial x}\frac{\partial\theta}{\partial\sigma}}^{x,t}} \underset{V}{+\overline{\frac{1}{c_p}\frac{\partial Q}{\partial x}}^{x,t}} \underset{VI}{+\overline{\frac{\partial}{\partial x}\left(\left.\frac{\partial\theta}{\partial t}\right|_{DIFF}\right)}^{x,t}} \underset{VII}{+\overline{\frac{\partial}{\partial x}\left(\left.\frac{\partial\theta}{\partial t}\right|_{CA}\right)}^{x,t}} . \quad (1)$$

The respective terms in this equation are (I): the quasi-Lagrangian tendency of cross-front temperature gradient, (II) confluence deformation acting upon the cross-front temperature gradient, (III) shearing deformation acting upon the along-front temperature gradient, (IV) tilting effects, and terms (V, VI, and VII) for the horizontal gradients of diabatic heating, horizontal diffusion, and convective adjustment.

Similarly, for the wind divergence budget, we have

$$\underset{I}{\overline{\frac{d}{dt}\left(\frac{\partial u}{\partial x}\right)}^{x,t}} = \underset{II}{-\overline{\left(\frac{\partial u}{\partial x}\right)^2}^{x,t}} + \underset{III}{f\overline{\frac{\partial v_{ag}}{\partial x}}^{x,t}} \underset{IV}{-\overline{\frac{\partial \dot{\sigma}}{\partial x}\frac{\partial u}{\partial \sigma}}^{x,t}} + \underset{V}{\overline{\frac{\partial}{\partial x}\left(\left.\frac{\partial u}{\partial t}\right|_{DIFF}\right)}^{x,t}} + \underset{VI}{\overline{\frac{\partial}{\partial x}\left(\left.\frac{\partial u}{\partial t}\right|_{PHY}\right)}^{x,t}}, \quad (2)$$

where the respective terms are: (I) the quasi-Lagrangian divergence tendency, (II) nonlinear divergence term, (III) unbalanced ageostrophic vorticity, (IV) tilting, (V) horizontal gradient of horizontal diffusion, and (VI) boundary layer frictional term. The strongest contributors to the low-level convergence feeding the updraft jet were the nonlinear and unbalanced ageostrophic vorticity terms, with the nonlinear effects dominating. Interestingly, the boundary layer effects were highly frontolytical at low levels, being related to the turbulent upward transport of easterly momentum within the updraft plume. Nonlinear effects became stronger than the ageostrophic residue effect in the later stages of frontogenesis in the DIFHT case, suggesting that an increasingly unbalanced frontal circulation developed *after* the time of maximum diurnal heating. Our results also showed that friction and mixing processes *weakened* the updraft due to the creation of low-level divergence, but the nonlinear convergence and ageostrophic vorticity terms were *augmented* as an *indirect* consequence of these viscous processes.

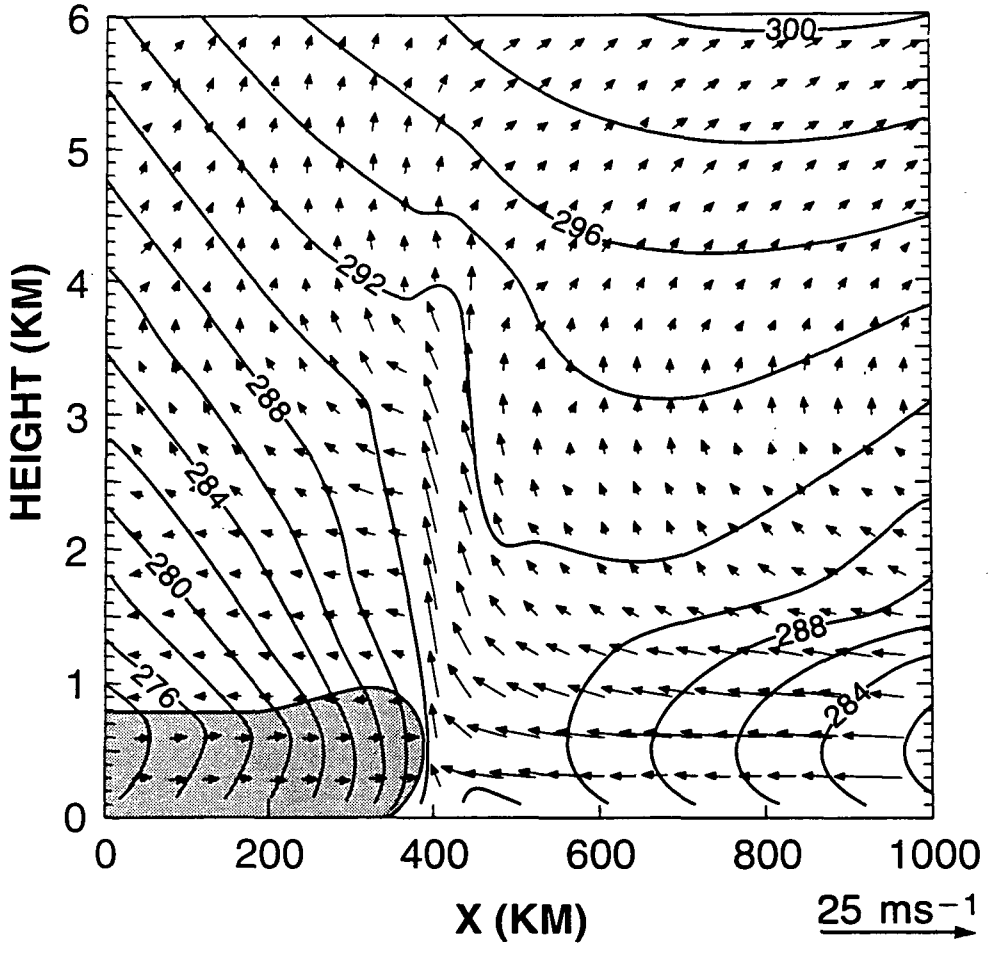

FIG. 2 Front-relative circulation and isentropes for differential heating experiment obtained from 7h forecast valid at 2100 UTC. Shaded region denotes area of positive front-relative flow (i.e., where $u_r > C$) indicative of density current structure. Maximum positive front-relative flow is 3.5 m s^{-1}.

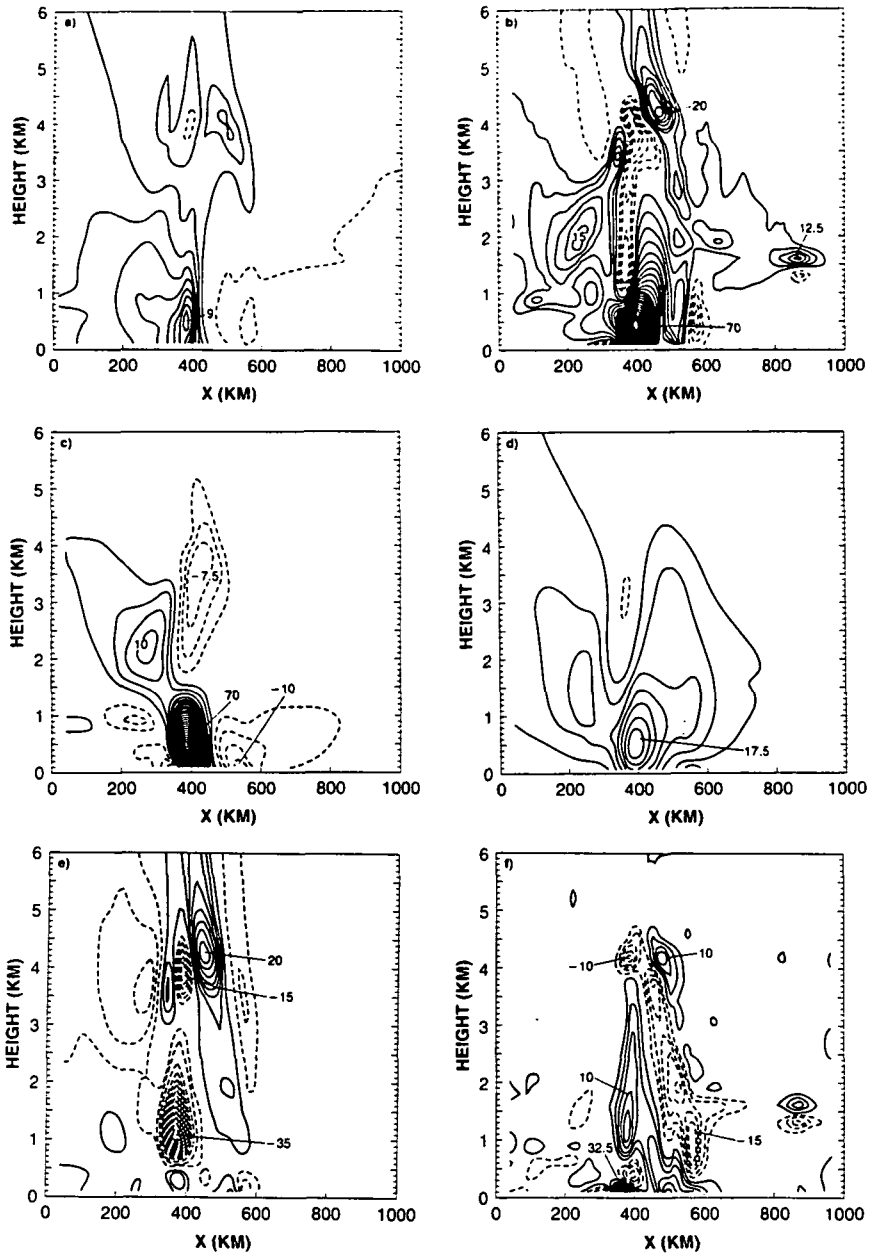

FIG. 3 Cross-front temperature gradient $\partial\theta/\partial x$ budget averaged over 1 hr and 80 km at 2100 UTC for differential heating experiment: (a) $\partial\theta/\partial x$ [contour interval 1K $(100\ km)^{-1}$]; (b) $d(\partial\theta/\partial x)/dt$; (c) $(\partial u/\partial x)(\partial\theta/\partial x)$; (d) $(\partial v/\partial x)(\partial\theta/\partial y)$; (e) $(\partial\dot{\sigma}/\partial x)(\partial\theta/\partial\sigma)$; and (f) the sum of terms V, VI, and VII in equation (1). Contour interval is 2.5 K $(100\ km)^{-1}$ $(day)^{-1}$ in all panels except (a), with positive (negative) values solid (dashed).

3. Task 2: Three-dimensional Simulation of an Observed Frontal Scale Contraction / Squall Line Event

3.1 Satellite-based humidity and soil moisture availability analyses

A simulation of the LC/CZ event reported by Koch (1984) was made using a three-dimensional version of the MASS model employed in the previous 2D study just described. A journal paper describing this research is presently in the review process (Koch et al. 1995b). A geostationary satellite-based cloud classification scheme was applied to the problem of specifying a detailed three-dimensional relative humidity field for the initial state of the model. A spatially variable soil moisture analysis derived from rain gauge data and fractional vegetation coverage obtained from polar orbiting satellite data was also employed. Volumetric soil moisture and vegetation fields were initialized into the MASS model following the method of Chang and Wetzel (1991).

Our method for enhancing atmospheric moisture detail in the initial state of the mesoscale model has important advantages. The dynamic clustering scheme (desBois et al. 1982) chosen to adapt to our needs has the unique combination of abilities to objectively define important cloud classes without any *a priori* assumptions, to distinguish cumulonimbus from thick cirrus and mixed-layer cloud decks, to detect differences in cloud fraction, and to use geosynchronous imagery to define cloud fields over land with 8 km resolution. The greatest uncertainty in our technique is the task of converting the cloud fraction for each of the cloud classes into vertical profiles of relative humidity RH, since the precise relationship between cloud fraction and RH has never been accurately established. A synthesis of the infrared satellite measurements, radiosonde humidity profiles, and surface cloud reports was employed to assign cloud depths for each cloud class. Special care was taken to insure that consistency was maintained between the moisture and thermal structures at all grid points.

The initial relative humidity (RH) fields at three isobaric levels and the surface moisture availability (M) fields are shown in Figs. 4 and 5, respectively. The top three panels in Fig. 4 show the RH fields produced without the benefit of the satellite moisture data. Those analyses rely entirely upon rawinsonde data and a coarse model "first guess" field. Notice the drying that has occurred in eastern Kansas in the mesoscale initialization. This region containing scattered cloud cover is just ahead of a strong cold front. The high contrast between this near absence of clouds ahead of the front and the overcast skies in western Kansas behind the front was hypothesized by Koch (1984) to be the essential driving force behind the development of the strong frontal circulation, since the radiative differences would create a strong cross-frontal gradient of sensible heating, which should strengthen the front (as indicated in the idealized modeling study above).

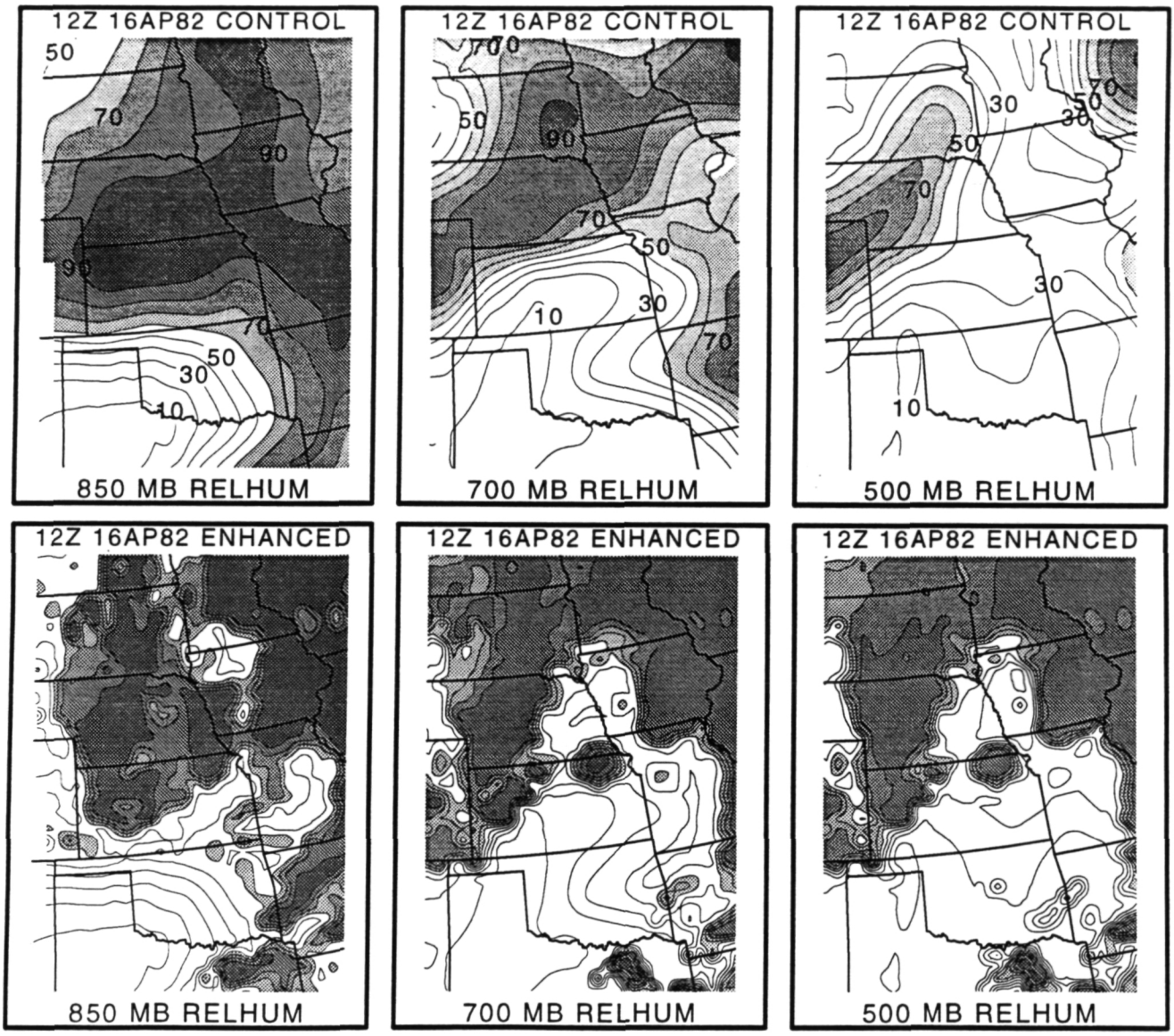

FIG. 4 Initial model fields of relative humidity at 850, 700, and 500 mb for the control case (top) and the satellite moisture "enhanced" case (bottom). The 48 km resolution enhanced analyses are derived from the cloud classification image and the cloud class humidity profiles, and were used for both the coarse and fine mesh grid resolutions. Shaded regions depict where clouds are diagnosed.

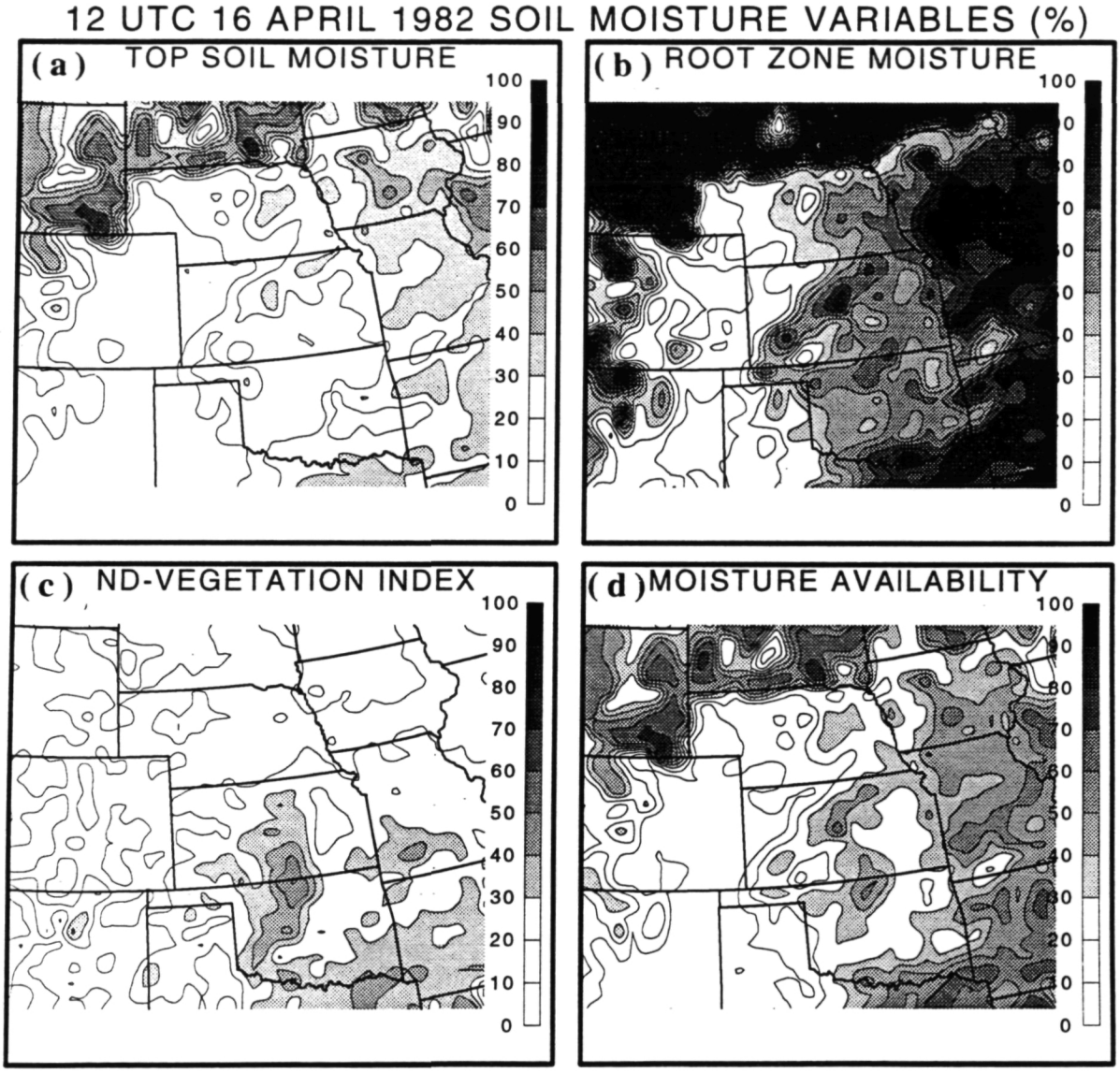

FIG. 5 Analyses of soil moisture content variables over the nested grid domain: top soil and root zone soil moisture (%), normalized difference vegetation index (NDVI), and resulting moisture availability M. Default value of moisture availability in MASS model is $M = 0.3$.

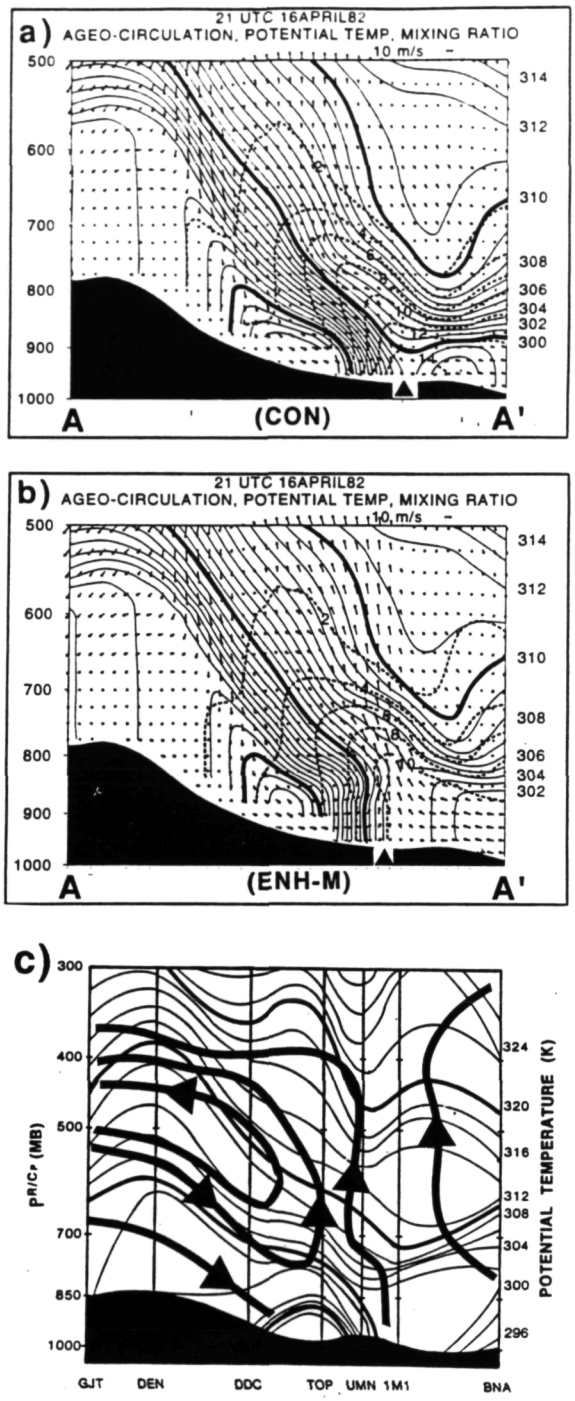

FIG. 6 Vertical cross sections perpendicular to cold front in eastern Kansas valid at 2100 UTC. Shown are forecast frontal transverse ageostrophic circulation (wind vectors), isentropes (^{o}K, solid lines), and isohumes (g kg^{-1}, dashed lines) from (a) control run and (b) enhanced run. Diagnosed surface position of front is depicted by triangle. (c) Isentropic cross section ($\Delta\theta$ = 2K) constructed from synoptic rawinsonde data at 00 UTC 17 April, along nearly the same line (after Koch (1984)), and ageostophic streamfunction obtained from Sawyer-Eliassen approach.

3.2 Dynamical effects of mesoscale moisture fields

The impact of the mesoscale initialization was investigated in several ways. The satellite-derived *RH* and *M* fields together led to >5K of warming and a dramatically increased boundary layer depth just ahead of the cold front. Thus, a strong cross-front pressure gradient was created in the region where the frontal squall line first formed. The mesoscale humidity field, and to a considerably lesser extent, the surface moisture availability gradient across the cold front, also resulted in the development of an erect frontal surface, a much stronger and deeper frontal updraft, and a density current-like "feeder flow" structure (Fig. 6). The latter feature occurred in response to the increased horizontal gradients in the sensible heating and pressure fields. These results are all consistent with the findings from the idealized frontal study (Task 1) showing the strong impact made by differential sensible heating. The satellite-based humidity data also resulted in a large improvement in the areal distribution and timing of mesoscale precipitation bands in the model forecasts. Accurate forecasts were made of the explosive frontal "squall line" only when the mesoscale initial fields were used.

These results strongly support the hypothesis of Koch (1984) that the nonlinear interaction between the adiabatic transverse frontal circulation and the thermally-forced circulation arising from the cross-frontal difference in cloud cover was the trigger for the frontal squall line. The moisture availability field provided secondary forcing, which indicates that mesoscale evapotranspiration fields can impact frontal behavior even in cases where strong dynamics are present.

This study points to the great need to execute special field experiments to develop verification databases for atmospheric and soil moisture fields, because there is no other way to definitively assess the accuracy of such fields for use in mesoscale models. The relatively simple technique used herein for inferring the evapotranspiration distribution in the model's initial state could be improved with future research that couples hydrological models with mesoscale atmospheric models to produce the initial conditions. This is desirable because of the paucity of soil moisture measurements over regional-scale areas. Another issue concerns the choice of model. Since a density current-like structure developed in our simulation, future modelling efforts should use fully nonhydrostatic physics and a bulk water continuity approach for explicitly predicting water substance instead of reliance upon a cumulus parameterization scheme. Finally, the application of the dynamic clustering scheme requires additional testing on other cases to address concerns related to the accuracy and reliability of the derived humidity fields, the method of data insertion, and other related issues. It is likely that preset *RH* profiles corresponding to unique bispectral or multispectral signatures of cloud classes can be defined to eliminate the need for repeatedly interpreting the cloud classes and for using surface and radiosonde data to provide the *RH* profiles.

4. Task3: Nonhydrostatic Frontal Modeling Effort

The findings from the idealized modeling study by Koch et al. (1995a) help to clarify several modeling and theoretical issues related to sensible heating effects on low-level frontogenesis. However, the relative importance of inhomogeneous heating was found to depend upon the grid resolution. These results emphasize the importance of using both high grid resolution and a multi-level PBL treatment to study cloud-induced sensible heating effects on frontogenesis. Although Koch et al. (1995a) suggest that differential cloud cover across cold fronts should promote the development of a microscale updraft of sufficient intensity to trigger frontal squall lines, the resolution of this issue awaits use of nonhydrostatic models with sufficient horizontal and vertical resolution, using second-order closure parameterizations of the boundary layer which allow for the coupling of cloud and boundary layer processes, and which include explicit prognostic equations for microphysics. The relative effects of turbulence, radiation, and subgrid scale cloud condensation were considered in the case of a stratocumulus-capped mixed layer by Chen and Cotton (1983). It would be of great interest to parameterize these effects (e.g., cumulus-induced subsidence and cloud top entrainment) into the boundary layer physics, since none of the simulations was successful at producing the strong microscale downdraft that Koch (1984) hypothesized was the cause for the observed post-frontal clear zone behind the cumulus line convection. Higher-order treatments of the momentum and heat fluxes in the PBL may be required to improve simulations of the turbulent structure during rapid frontogenesis.

There are three scientific purposes of this research. First and foremost is to understand whether the interaction between a thermally-forced circulation arising from the cloud cover and the adiabatic frontal scale contraction can produce a sufficiently strong frontal updraft to initiate deep convection as observed in line convection cases by the P. I. in circumstances where the Convective Available Potential Energy is high (Dorian et al. 1988). This objective could not be attained with the coarser hydrostatic modeling study which neglected moisture processes (Koch et al. 1995a). Secondly, the inclusion of sophisticated PBL and moisture physics will permit, for the first time, a study of the relative importance of adiabatic frontal scale contraction (the Eliassen self-sharpening process), diabatic processes related to boundary layer processes (the thermally-forced circulation), and precipitation processes (e.g., melting and evaporation) in the development of a density current structure at the leading edge of cold fronts, and also the formation of intense narrow cold frontal rainbands. Thirdly, we wish to include cumulus cloud-PBL-radiative flux interactions to investigate the possible role of cumulus-induced mass fluxes and compensating subsidence in the creation of the line convection and clear zone, respectively, and the possibility that cloud top radiative cooling and in-cloud warming effects could be important to the dynamics of this kind of boundary layer.

A two-dimensional, nonhydrostatic numerical model containing high horizontal resolution, sophisticated planetary boundary layer (PBL) processes, and explicit moisture processes is required. We have adapted the model developed by Dr. Chaing Chen at NASA/Goddard for these purposes (Chen 1991; Chen et al. 1994). This terrain-following coordinate, anelastic model includes the Duynkerke and Driedonks (1987) planetary boundary layer scheme, non reflective open lateral and upper boundaries, a grid nesting scheme that employs radiative boundary conditions and blending of inner and outer grid tendencies, and both warm rain and ice microphysical processes following Proctor (1987a, b). The PBL scheme is a multilevel, ensemble-averaged model formulated using the turbulent kinetic energy equation and a parameterized version of the energy dissipation equation. It is particularly well suited to the study of cloud-topped PBLs and the effects of clouds on turbulent fluxes within the PBL, since it includes not only upward buoyancy flux at the surface, but also the longwave radiative cooling near the cloud top, shortwave radiative warming in the cloud, and wind shear at the top of the PBL. These processes can lead to a decoupling of the cloud layer from the subcloud layer, enhanced entrainment of warm, dry air at the cloud top, and other realistic effects without resorting to expensive large-eddy simulations.

We have installed this model, with the help of Dr. Chen, on the CRAY Y-MP at the North Carolina Supercomputing Center. We have worked on a frontal initialization scheme for the model. The inclusion of a realistic upper-level front requires that we choose an initial state that has vertical shear of the horizontal wind, and an associated horizontal temperature gradient (i.e. a baroclinic basic state). An idealized representation of a front that would intensify through shearing deformation should allow us to specify a fairly realistic initial condition. This technique has been widely used in previous theoretical studies of the frontogenesis processes, including Koch et al. (1995a). The results from the Eady model at t=60 hr and 77 hr are shown in Fig. 7. An idealized front has formed and intensifies with integration time, as expected. The intensification during this 17-h time period of the cross-front temperature gradient, the vorticity of the alongfront flow, and the direct secondary circulation revealed in part by the vertical motion field w are all a response to the frontogenetical process whereby horizontal shearing deformation acts upon the alongfront temperature gradient.

The method of frontal initialization described by Reeder and Smith (1987) has also been adapted for this project, because it allows one to specify virtually any kind of frontal structure due to its generality. In addition, stability can be specified as being non-uniform, which allows for easy incorporation of potential vorticity anomalies. Although we have developed the equation set for this frontal initialization, more time is needed to code and test the frontal initialization model. With the ending of funding prospects from NASA for this research, we abandoned this task at this point and instead concentrated our efforts at successfully completing Task 4 described below.

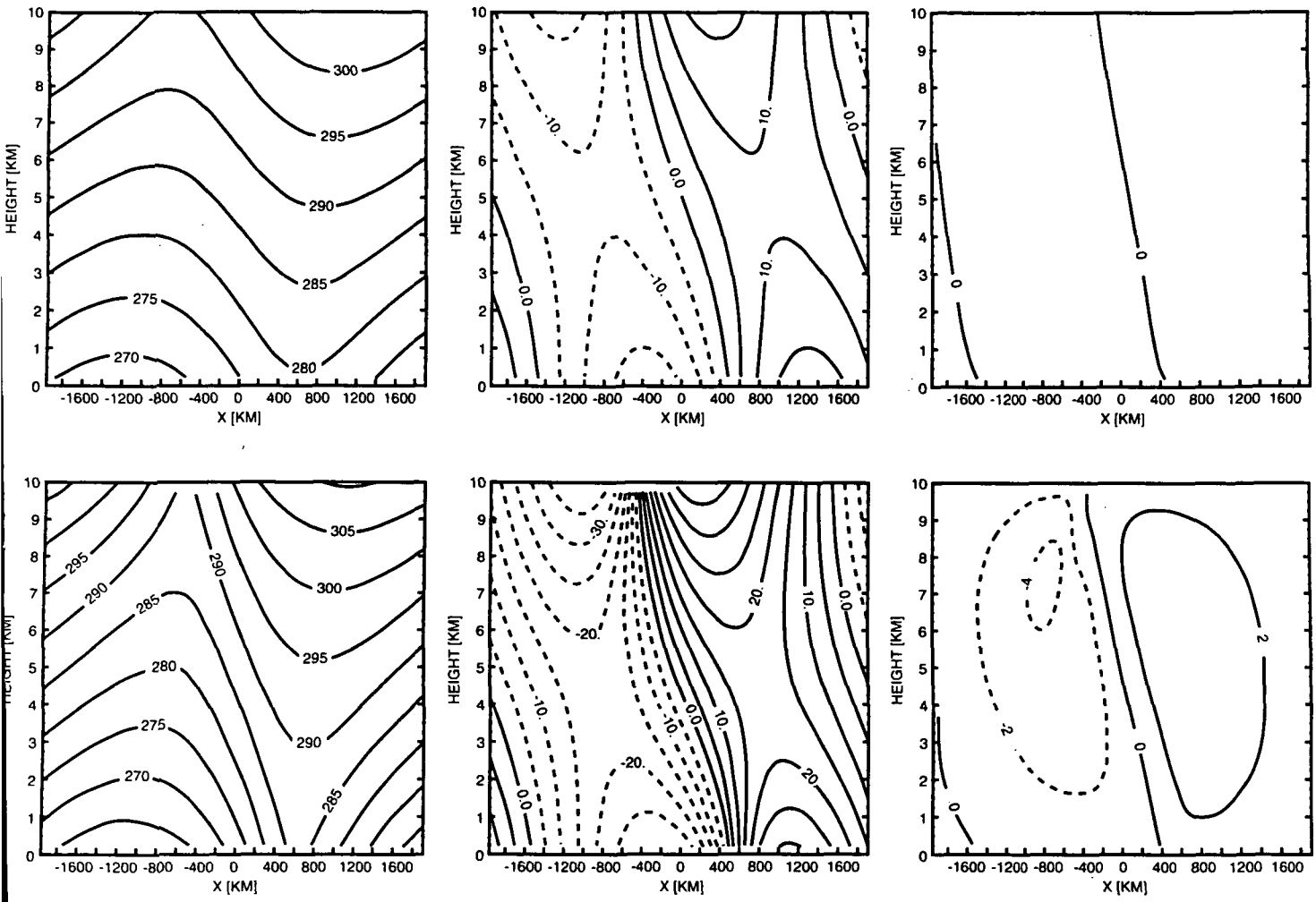

FIG. 7 Cross sections of: numerically predicted potential temperature θ (left, contour interval 5 K), alongfront wind v (middle, contour interval of 5 m s^{-1}, with northerly winds dashed), and vertical velocity w (right, contour interval 2 cm s^{-1}, with downward motions dashed). Top (bottom) panels are from t = 60 h and 77 h, respectively.

5. Task 4: Modeling of Observed Density Current - Gravity Wave Interactions

Frontal scale contraction can take various forms. The LC/CZ and NCFR cloud features are two examples of meso-gamma to meso-beta scale frontal circulations that each display some features characteristic of gravity (density) currents. Gravity currents are capable of producing gravity waves when the right environmental conditions are met. There have been numerous observational studies (Charba 1974; Marks 1974; Goff 1975; Doviak and Ge 1984; Fulton et al. 1990; Koch et al. 1991), laboratory models (Rottman and Smith 1985), and numerical simulations (Wakimoto 1982; Droegemeier and Wilhelmson 1987; Haase and Smith 1989; Raymond and Rotunno 1989; Lin and Chun 1991) of gravity currents and associated gravity wave activity. An undular bore is an example of one such wave disturbance, and evidence for the existence of such a phenomenon along an intense cold front observed during COPS-91 is examined in Task 5. Other gravity wave phenomena that can be excited by the passage of a density current into a stably stratified atmosphere include solitary waves and Kelvin-Helmoltz waves.

Gravity waves will be incoherent, short-lived phenomena in the absence of some means to trap the upward leakage of wave energy in a stratified atmosphere. Three wave trapping mechanisms were proposed by Crook (1988): (1) the curvature in the velocity profile associated with a low-level jet opposing the wave motion, (2) winds in the mid- to upper-troposphere opposing wave motion, and (3) a mid-tropospheric inversion found at a height of one quarter of a vertical wavelength above a surface-based stable layer.

Recently an observed gravity current and its associated gravity waves have been studied in unprecedented detail by Ralph et al. (1993) (hereafter referred to as R93). The combined use of two Doppler sodars and a 45-MHz wind profiler enabled them to achieve incomparable vertical profiling from the surface to nearly 10 km above ground level (AGL) at very high sampling (4 s to 2 min) intervals. Both the gravity current and a variety of gravity waves were clearly documented by combining those data with more conventional meteorological data. One unique feature suggested by the observations was lee-type waves forced by the gravity current acting as an obstacle to the prefrontal

low-level inflow (R93). However, it remains to fully understand the origins and structures of the disturbances associated with the gravity current as proposed in their study. The observations contained very limited information about horizontal motion or temperature fields, no direct measurements of wavelength and phase speed, and an 800 m data gap existed between the sodars (19-476 m AGL) and the wind profiler (>1.2 km), which probably prevented measurement of the strongest upward motions within this layer.

For these reasons, we have used a primitive equation model to test the tentative hypotheses developed from the observational analyses and to "fill in" gaps in space and time. Numerical simulations of the observed gravity current and its associated gravity waves were made using the two dimensional, nonhydrostatic, dry model of Chen (1991). Wave origins and propagation mechanisms were also investigated to test the hypotheses proposed by the observational study. The results of this research have been submitted for publication (Jin et al. 1995).

Two sets of grid mesh were tried for the simulations. The resolution of the fine grid mesh was Δx=200 m, Δz=50 m with 1026 grid points in the horizontal direction and 101 in the vertical. To generate the propagating gravity current, a strong steady-state surface heat sink (cooling rate=34 k hr^{-1}) of 5 km width and 2.8 km depth was incorporated into the model which is ascribed to the evaporative cooling of precipitation in the subcloud layer (Lin and Chun, 1991). The initial sounding for the model control runs was a composite sounding which consists of soundings of 5 hours before the front passed and the soundings just after it passed as suggested by the observational analyses. This sounding contains a shallow inversion layer (250 m) above the surface, a weakly stable layer, and two neutral layers at higher levels. The initial wind profile contains an easterly flow below 1.7 km with the maximum wind speed of 7.5 m s^{-1} near the surface, whereas flow changes into westerly flow at high levels (above 1.7 km). Except for the thin layers of strong curvature at low levels, the wind profile is basically composed of two layers of linear shear with a strong curvature point at the interface of the two layers at z=3.1 km.

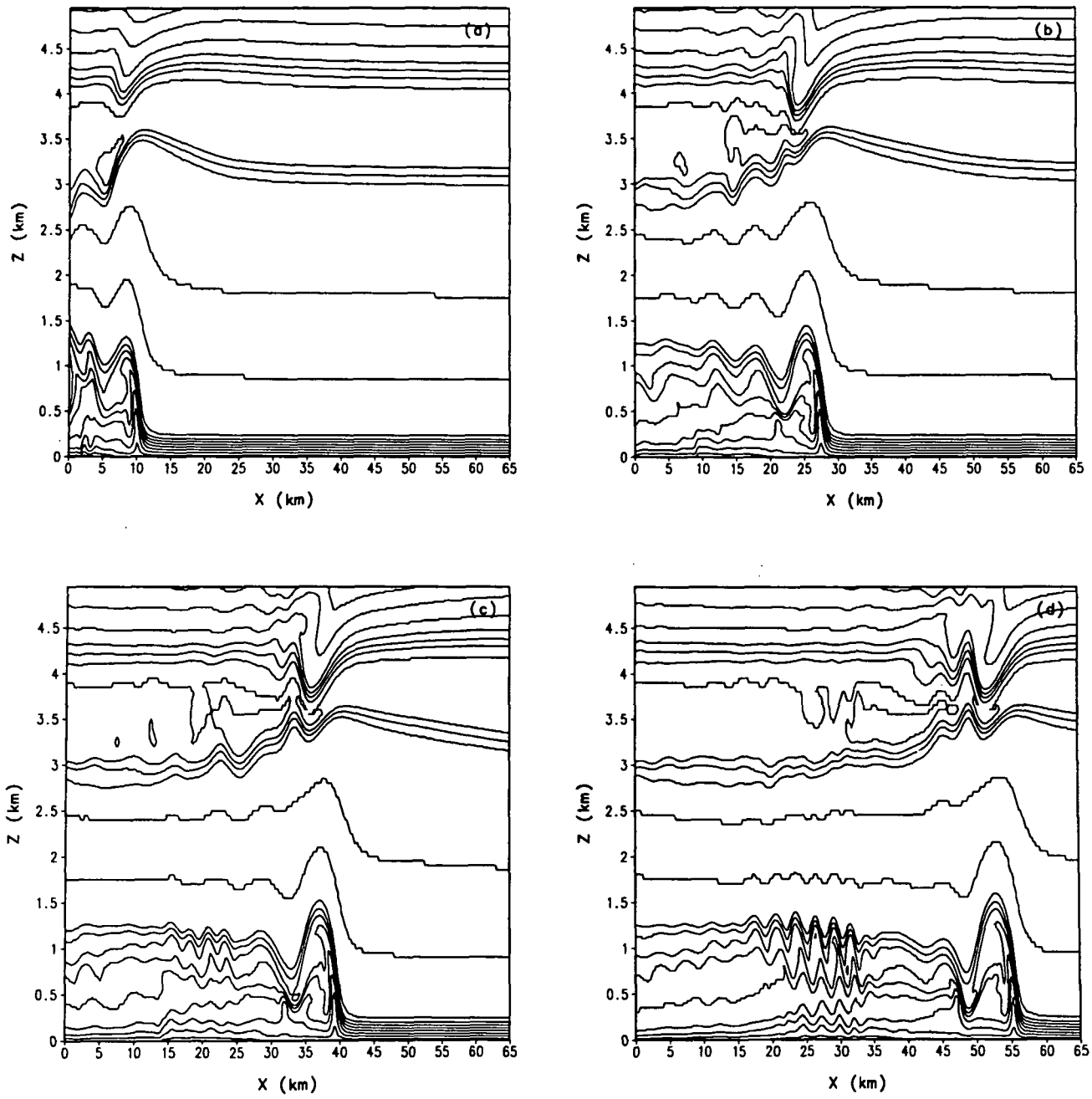

FIG. 8 Simulated potential temperature fields (contoured at intervals of 1 K) for the control run with the fine resolution at (a) t=0.5 hr; (b) t=1.0 hr; (c) t=1.37 hr; (d) t=1.75 hr.

The atmospheric response to the surface heat sink bears characteristics of a gravity current which moves at the same speed as observed (C_{gr}=10 m s^{-1}). Fig. 8 shows the numerically simulated potential temperature fields at different model times with the fine resolution. The distribution of isentropes indicates that the depth of the gravity current is about 1.4 km. Air immediately behind the front is averagely 4 degrees cooler than that before the gravity current up to 1.2 km. These modeled characteristics reproduce those observed in R93 several minutes after the front passed. The greatest temperature contrast across the head of the gravity current reaches 6 ^{0}C at about 500-m level in the simulation, which was not resolved by the observations. The simulated u wind field (not shown) shows a well-defined wind reversal clearly marking the gravity current within the lowest 1 km. The strong easterly flow is elevated by the intrusion of the cold air resulting in significant vertical shear of the horizontal wind there, i.e., 14 m s^{-1} within 500 m. This shear is considered to be the major mechanism for K-H waves appearing in this region (further discussions later).

Strongest upward motion is centered on the upstream side of the leading edge of the gravity current with values increasing from zero at the surface to greater than 3 m s^{-1} at about 300 m, as observed. Also found in the simulation results is that the strong vertical motion for the gravity current is confined to altitudes below 3.5 km, the same as that deduced by R93 from the wind-profiler vertical velocity data. The vertical extent of the updraft was suggested by R93 to be limited by the neutral layer just below 700 mb. This is the probable explanation for the fact that deep convection did not develop from the lifting along the gravity current head. Absent in the observational analyses is the simulated maximum value of 6.3 m s^{-1}, which is as much as 3 m s^{-1} greater than the observed maximum value. This disagreement can be attributed to the aforementioned observation gap since the simulated maximum value happens to lie at the altitude of 1 km within the gap. It is also possible that the 2-min averaging by the wind profiler misrepresented the actual maximum updraft speeds. One feature common to gravity currents, i.e., the overturning circulation within the gravity current head, is also captured by the simulation.

The other significant features in the fine resolution run are gravity waves distorting both the upper boundary of the gravity current and the regions above the cold air behind the gravity current head. To investigate the possible mechanisms for wave origin and propagation, parameter m^2 and the Richardson number R_i are calculated. The equation determining the vertical wave number (m) is:

$$m^2 = \frac{N^2}{(u-c)^2} - \frac{\partial^2 u/\partial z^2}{u-c} - k^2 = l^2 - k^2 \tag{3}$$

where $u-c$ is the horizontal wind relative to the propagating speed of the gravity wave (c); N the Brunt-*Väisälä* frequency, $\partial^2 u/\partial z^2$ the curvature in the wind profile, k the horizontal wave number, l the Scorer parameter, and z the altitude:

$$l^2 = \frac{N^2}{(u-c)^2} - \frac{\partial^2 u/\partial z^2}{u-c} \tag{4}$$

Based on the Goldstein-Taylor equation, a wave with $m^2 > 0$ can propagate vertically; a wave with $m^2 < 0$ is evanescent because its amplitude decays exponentially with height. The Richardson number is determined as:

$$R_i = \frac{N^2}{(\partial u/\partial z)^2} \tag{5}$$

The Miles theorem (Miles 1961) states that $R_i < 0.25$ is the necessary condition for Kelvin-Helmoltz (KH) instability.

Notice in Figs. 8a and 8b the presence of three or four distinct undulations trailing the head of the gravity current, which have a wavelength of ~6.8 km. Similar undulations are found between 0.5 and 3.0 km, and represent vertically oriented phase lines, a characteristic of trapped waves. This structure closely resembles the structure documented by observations in terms of the lack of phase tilt and the vertical extent of the undular perturbations. This represents strong validation of this aspect of the simulation, indicating that the model can be used to further test the wave generation hypothesis. According to this trapped lee-wave hypothesis, the wave should be motionless relative to the gravity current head. This behavior could not be observed, but is present in the simulation, in which these waves travel at 8.8-10.7 m s^{-1}, which is close to the gravity current propagation speed of 10.0 m s^{-1}. The

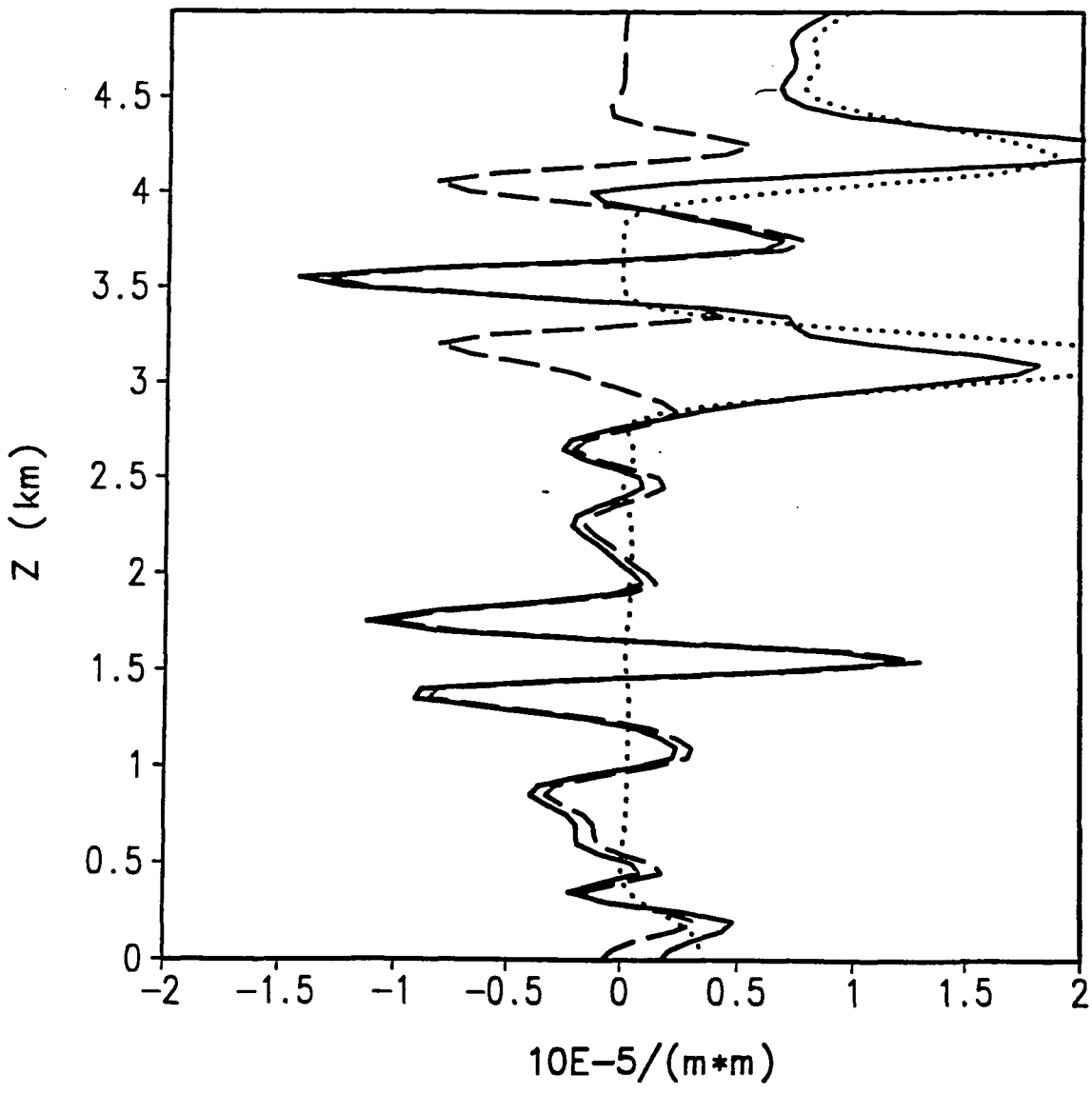

FIG. 9 Profile of square of the vertical wave number (solid line) at initial time for the control run. The dashed and dotted lines are contributions of the curvature term $-u''/(u-c)$ and term $N^2/(u-c)^2$ respectively.

m^2 distribution as shown in Fig. 9 can be considered to be composed of three pairs of lower and upper layers based on the associated wave activities. For each of the three pairs, layer-averaged m^2 is positive and negative for the lower and upper layers respectively, which makes it possible for internal wave modes to exist in the lower. Furthermore the necessary condition for the existence of trapped lee-waves for the two-layer problem:

$$l_L^2 - l_U^2 > \frac{\pi^2}{4H^2}, \tag{6}$$

where l_L and l_U are the Scorer parameters in the upper and lower layers, respectively, and H is the depth of the lower layer (Scorer 1949), is well satisfied for the third layer pair with the left-hand side nearly one order of magnitude greater than the right-hand side. This analysis attests to the existence of a wave trapping mechanism, and strongly supports the interpretation by R93 that the waves observed within the layer between 1.2 and 3 km are trapped lee-type waves.

As the model is integrated to t=1.27 hr, waves of shorter wavelengths begin to develop at the interface between zone IIc and zone I (not shown). At t=1.37 hr these waves are evident only in the region at z=1 km about 20 km extending behind the leading edge of the gravity current (Fig. 8c). The evolution of the Richardson number distribution (Fig. 10) indicates that the shorter waves do not develop until the regions of possible dynamic instability get to a certain size. Short waves are generated in the region of $R_i < 0.25$ collocated with regions of strong vertical shear between the pre-frontal easterly flow forced above the gravity current and westerly flow of the cold air consisting of the gravity current. Thus, it can be inferred that the main cause for the possible dynamic instability is shear instability and the waves are shear induced KH waves. After the KH instability grows, the regions of $R_i < 0.25$ become enhanced and focused into smaller scales by the short KH waves. The wave periods of 15 min and 20-23 min fall exactly in the observed 14-22 min range of wave periods. The estimated wavelength (2.9 km) compares well with the simulated values (2.2-2.7 km). The KH instability perturbs not only the layer at the interface, but also the layers above and below.

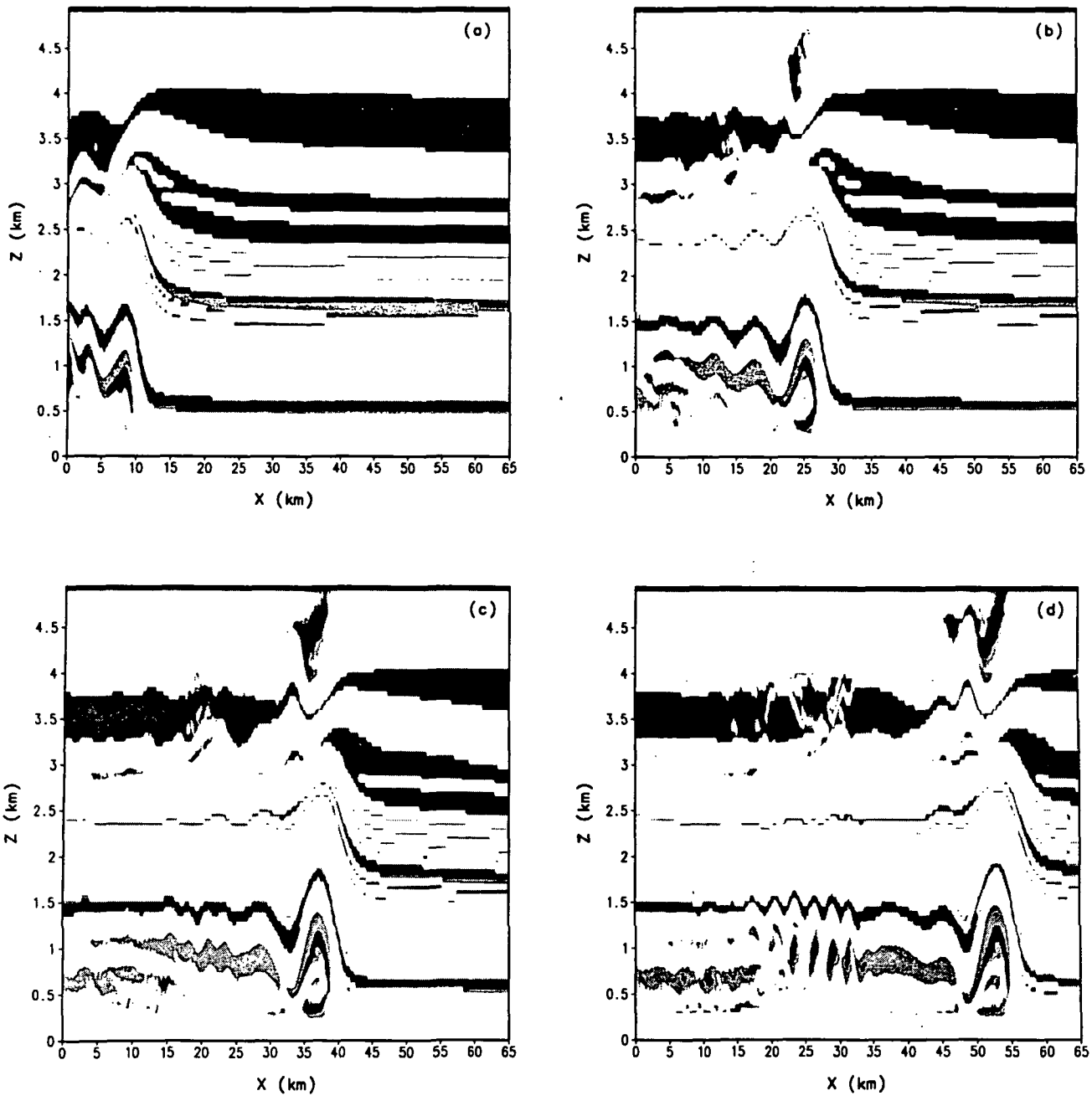

FIG. 10 Distribution of the R_i number for the fine resolution run with regions of R_i <0.25 light gray shaded and regions of R_i <0 dark gray shaded at (a) t=0.5 hr, (b) t=1.0 hr, (c) t=1.37 hr, and (d) t=1.75 hr.

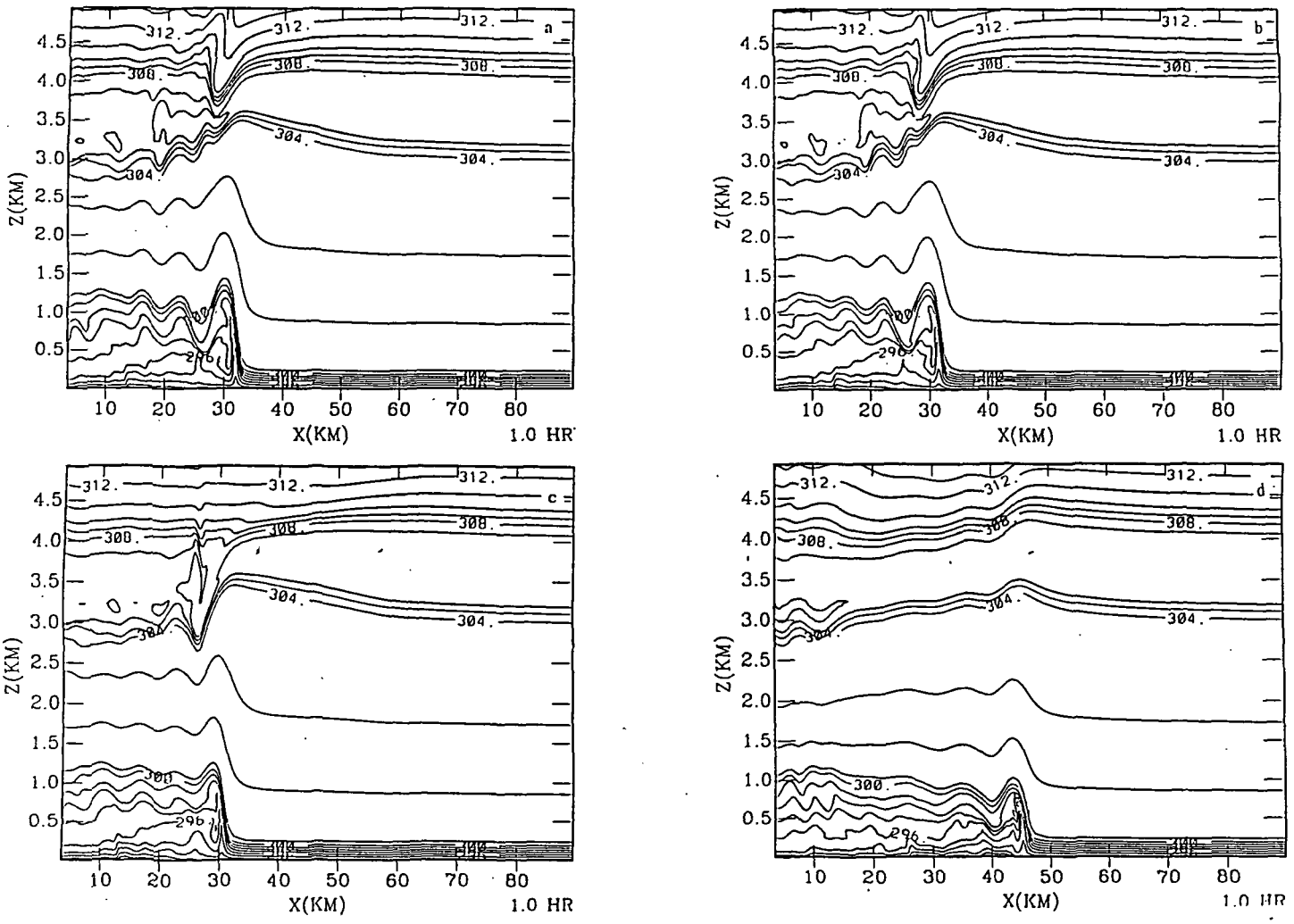

FIG. 11 Isentropes (K) at t=1 hr for: (a) the control run (CR); (b) test SP; (c) test LS; (d) no initial wind (NW) test. (Fine resolution model).

Because of the good agreement between the observations of the gravity current and its associated gravity waves, the model is used here to thoroughly test the conclusions concerning the wave trapping mechanism that led to the existence of the trapped lee-type waves. Three different initial wind profiles were tested for the wave trapping mechanisms. When the environmental wind profile is modified so as to eliminate small variations that create curvature at low levels, but retain the significant curvature near 3.1 km AGL (test SP), the lee-type waves remain essentially unchanged (Fig. 11b). When the curvature is removed from the entire wind profile (test LS), but the low-altitude opposing flow is retained, the wave amplitude is significantly reduced (Fig. 11c). This result lends further support for the argument made before that only the curvature aloft (near 3.1 km) is important for wave trapping based on the examination of m^2 profile (Fig. 9). When the environmental wind is set to zero, both the curvature and the low-altitude opposing flow are removed (test NW), resulting in even weaker waves and a faster gravity current propagation speed (Fig. 11d). These simulations confirm that the curvature aloft in the wind profile has an important effect on wave trapping in this case, a conclusion consistent with the results from other cases studied by Crook (1988), and the strong bore case of Koch et al. (1991).

Nevertheless, both the observed coincidence of the sudden weakening of wave amplitudes with the existence of the isothermal layer above 3.3 km and the dominance in the m^2 profile by the contribution from the term $N^2/(u-c)^2$ within the isothermal layer suggest that the isothermal layer may contribute significantly to trapping the waves. A sensitivity test (NISO) is run for this purpose by removing the isothermal layer at about 3.4-3.7 km but maintaining the same lapse rate elsewhere in the initial sounding as that for the control. This change in the initial sounding significantly modifies the wave behavior. The wavelength is reduced to about 4 km in the lower layer and causes m^2 to be significantly different from l^2 (Fig. 12). The entire negative m^2 layer from 0.3 km to 4 km indicates that the wave is evanescent in this layer. The isothermal layer helps to trap the wave energy in two ways, by: (1) making the horizontal wavelength long enough ($m^2>0$) so that the waves can propagate in the wave duct; and (2) causing a strong positive m^2 layer just below the negative m^2 associated with the strong curvature aloft in order for wave activities to be clearly seen until just below the layer of negative m^2. Thus the elevated isothermal layer and the curvature act together to maintain the trapped lee-type waves.

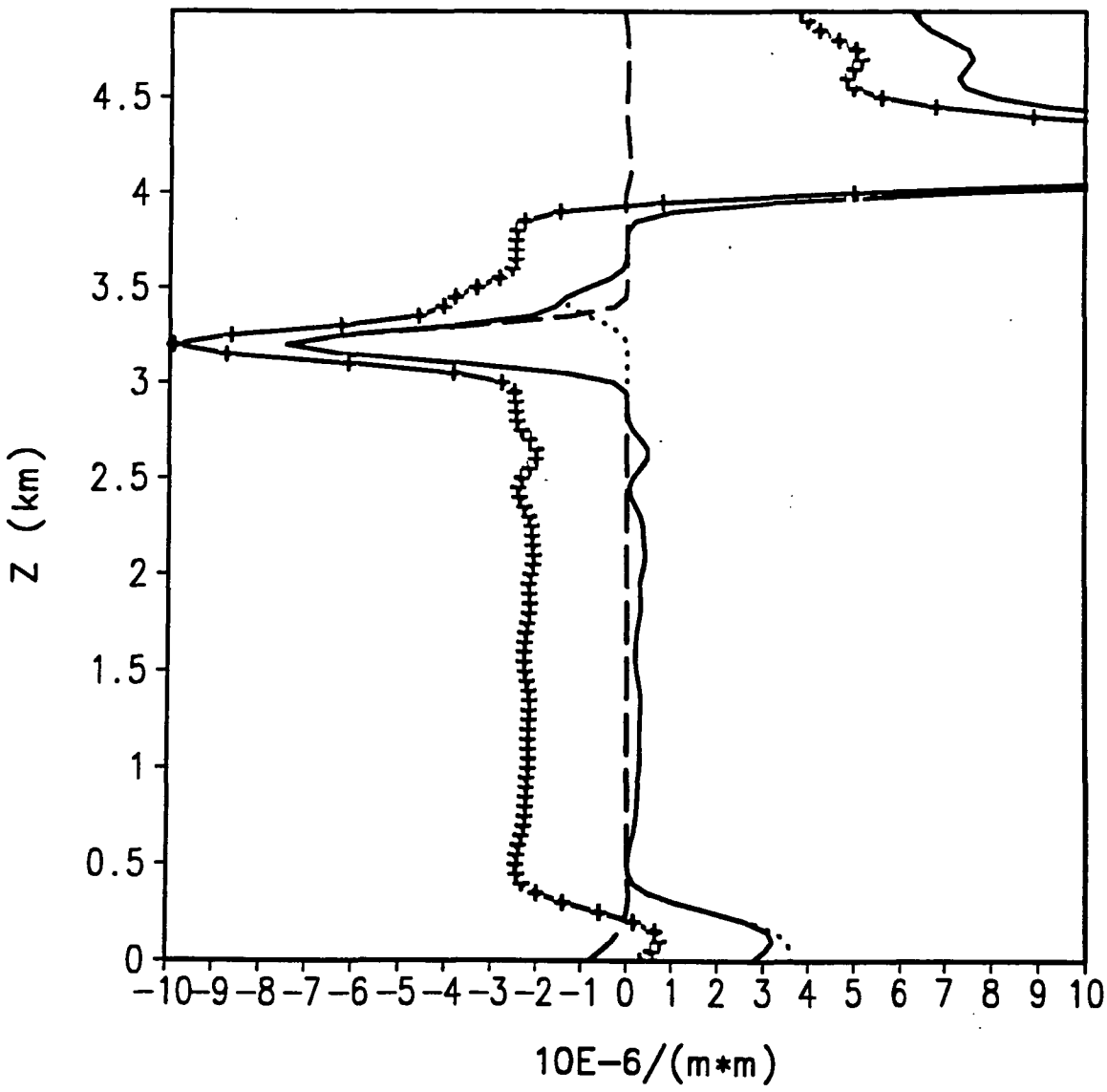

FIG. 12 Profile of square of the Scorer parameter (solid line) at initial time for the NISO test. The dashed and dotted lines are contributions of the curvature term $-u''/(u-c)$ and term $N^2/(u-c)^2$ respectively. The crossed line is the m^2 profile.

Also in agreement with the observations in R93, the model simulations show no evidence of a bore propagating ahead of the gravity current, even though the gravity current is entering into an environment with conditions often considered conducive to bore generation, i.e., the low level stability and low level jet together with the curvature aloft (Doviak and Ge 1984; Simpson 1987; Crook 1988; Koch et al. 1991). In the observational paper it was concluded that the stable layer near the surface was not deep enough for a bore to develop. Sensitivity tests were performed to test this hypothesis by systematically increasing the depth of the low-altitude stable layer using the coarse resolution domain. It was found that there is a tendency for a bore-like disturbance to develop and leave behind a much weakened gravity current as the depth of the stable layer increases.

In summary, the gravity current produced by the cooling in the model bears remarkable similarity to the observed event, including its propagation speed, the wind shift, the depth of the cold pool, and the temperature drop across its leading edge. Not only are the gross features of the gravity current well simulated, but so are two classes of gravity waves triggered by the gravity current and uniquely documented in the observational study (R93), namely the train of trapped lee-type gravity waves produced by flow over the gravity current head, and Kelvin-Helmholtz waves that form on the interface atop the cold pool. Sensitivity tests further support the hypothesis suggested form the observations that gravity wave propagation speed in the stable layer must exceed the gravity current propagation speed and that the prefrontal near-surface stable layer was too shallow to allow for the production of such a wave. Future studies using both ground-based and airborne remote sensing techniques are likely to further our observational documentation of these interesting mesoscale structures. By combining such observational studies with detailed numerical simulations, such as done here, even greater understanding of the underlying physical processes may be gained. It is also hoped that further theoretical studies on dynamic instability should give more accurate quantitative relationship between the wavelength shortening and area of the small Richardson number (R_i <0.25) in order to predict wave evolution.

6. Task 5: Analysis of a Bore-like Front in the COPS-91 Field Project

Processes that produce narrow convective lines along intense cold fronts can be better understood with detailed observations from multi-scale field experiments which have a strong remote sensing component, as in the Cooperative Oklahoma Profiler Studies (COPS-91). This field program included as one of its major components documentation of the structure and dynamics of dry fronts and associated mesoscale phenomena. Surface mesoscale PAM stations, WSR-88D and dual-Doppler radars, 405 and 915 MHz wind profilers, a microwave radiometer for sensing water vapor and cloud properties at Amber, Oklahoma, and other systems were deployed. The merger of a cold front with a stalled dryline and the rapid evolution of the merged system into a density current-like microstructure with a prefrontal bore were documented during the evening of 26 April 1991 (following the infamous Andover, Kansas tornado outbreak). This scale-contracted front played a key role in triggering the formation of a second outbreak of severe weather that evening. The analysis of the data from this event have been analyzed completely. The results have been presented at a conference (Koch et. al. 1994) and are presently being written as a journal paper.

The COPS-91 field program (Hane et al. 1993) included as one of its major components documentation of the structure and dynamics of dry fronts and associated mesoscale phenomena. An extremely interesting frontal event occurred on the evening of the infamous Andover, Kansas tornado outbreak. Satellite imagery at 0200 UTC 27 April 1991 shows a large convective complex in eastern Kansas and western Missouri that contains the remnants of the Andover storms, but also a newly developing system along the cold front in southern Kansas (Fig. 13). This new squall line eventually built southward into central Oklahoma as the cold front merged with the stalled dryline. Note that the dryline is not convectively active, nor is there much confluence along it. The surface data (including a dense network of 7 PAM stations centered about Amber (Fig. 14)) and WSR-88D radar imagery reveal that the dryline never made it into the region near Amber, even though from Fig. 13 it might appear that the the storms developed at the dryline-cold front merger. This display and the accompanying radial velocity fields (not shown) reveal a single convergence boundary associated with the cold frontal system stretching across the center of the state, but no indication of the dryline due to the lack of convergence along it. The WSR-88D and the Norman NSSL Doppler radars show that this single fine line evolved into a double system (a density current and bore) as the cold front passed through the Amber region, and that the bore increasingly separated from the front with time (Fig. 15). Severe storms began developing within minutes along the density current-like front (the westernmost fine line) from just south of Enid. The southernmost point of this new squall line was *considerably* north of the dryline-front merger point, which was somewhere in the FSI area (Fig. 14). It is fascinating that *the squall line developed only along that part of the frontal system that displayed this double structure* as evident in the Doppler radar, PAM, and radiometer data.

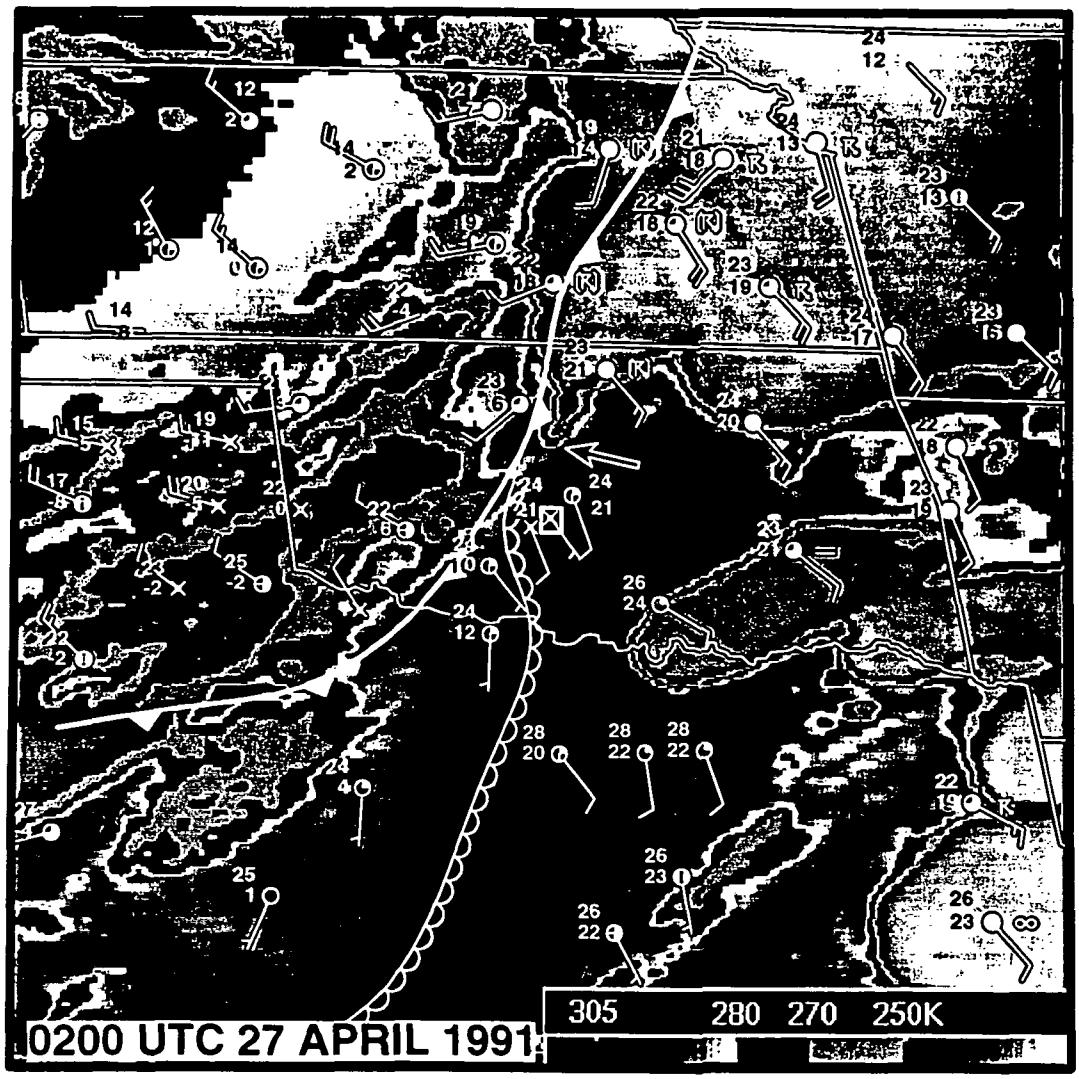

FIG. 13 GOES enhanced infrared imagery and surface (NWS plus some PAM stations) data (temperature and dew point (oC) and present weather) at 0200 UTC 27 April 1991. Arrow denotes tail end of flanking line of newly developing severe storms. Small box just south of arrow is Amber, OK. The cold clouds in the Texas Panhandle are not convective, but rather are thick cirrus clouds.

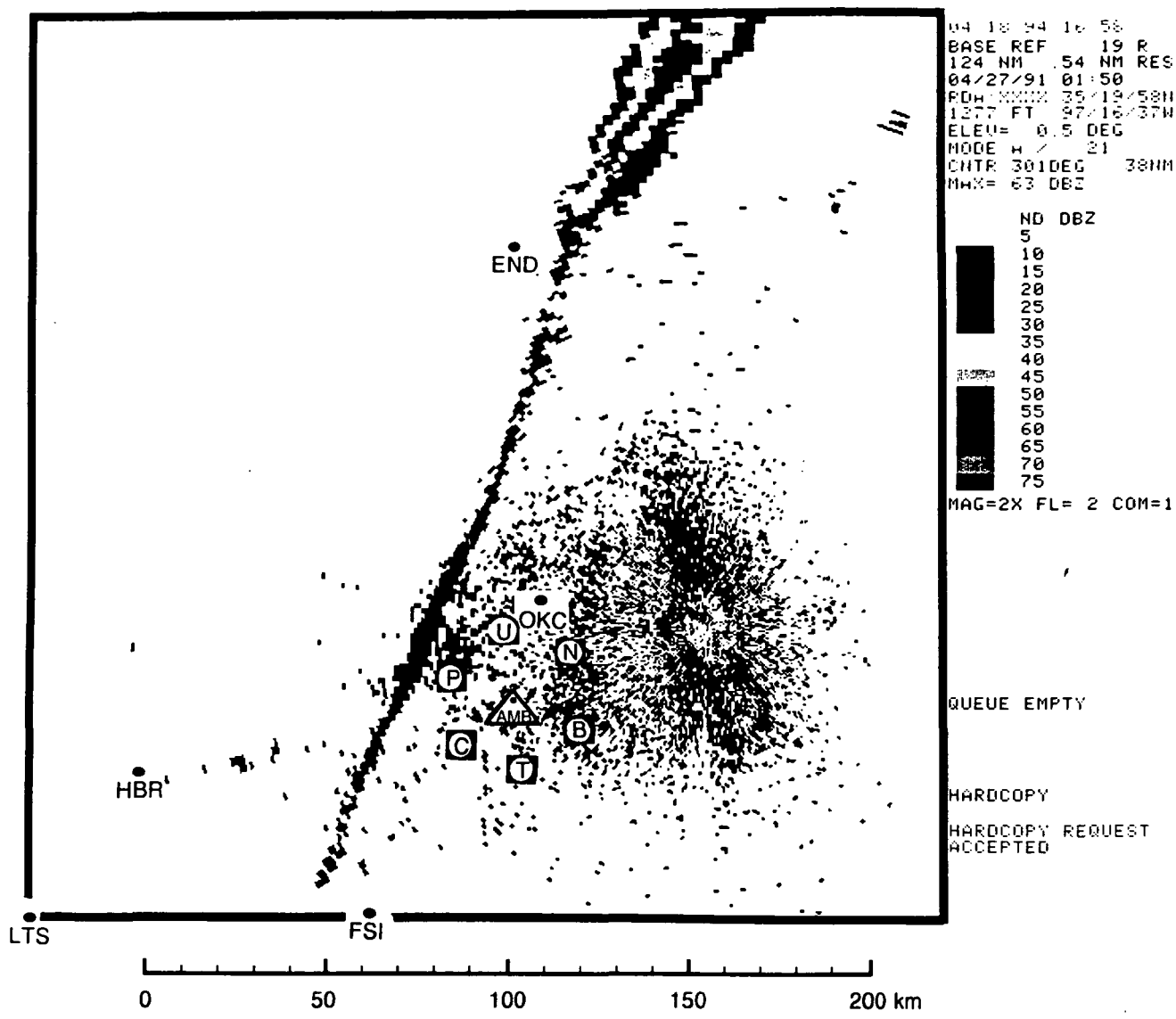

FIG. 14 KOKC WSR-88D base reflectivity imagery (0.5° elevation angle) at 0150 UTC. Note new squall line (55 dBZ) building southward from northern Oklahoma near Enid, the 15 dBZ "thin line" of reflectivity stretching southwestward from the squall demarcating the cold front, and the location of Amber and surrrounding PAM stations. and the Norman Doppler radar coverage (rectangle).

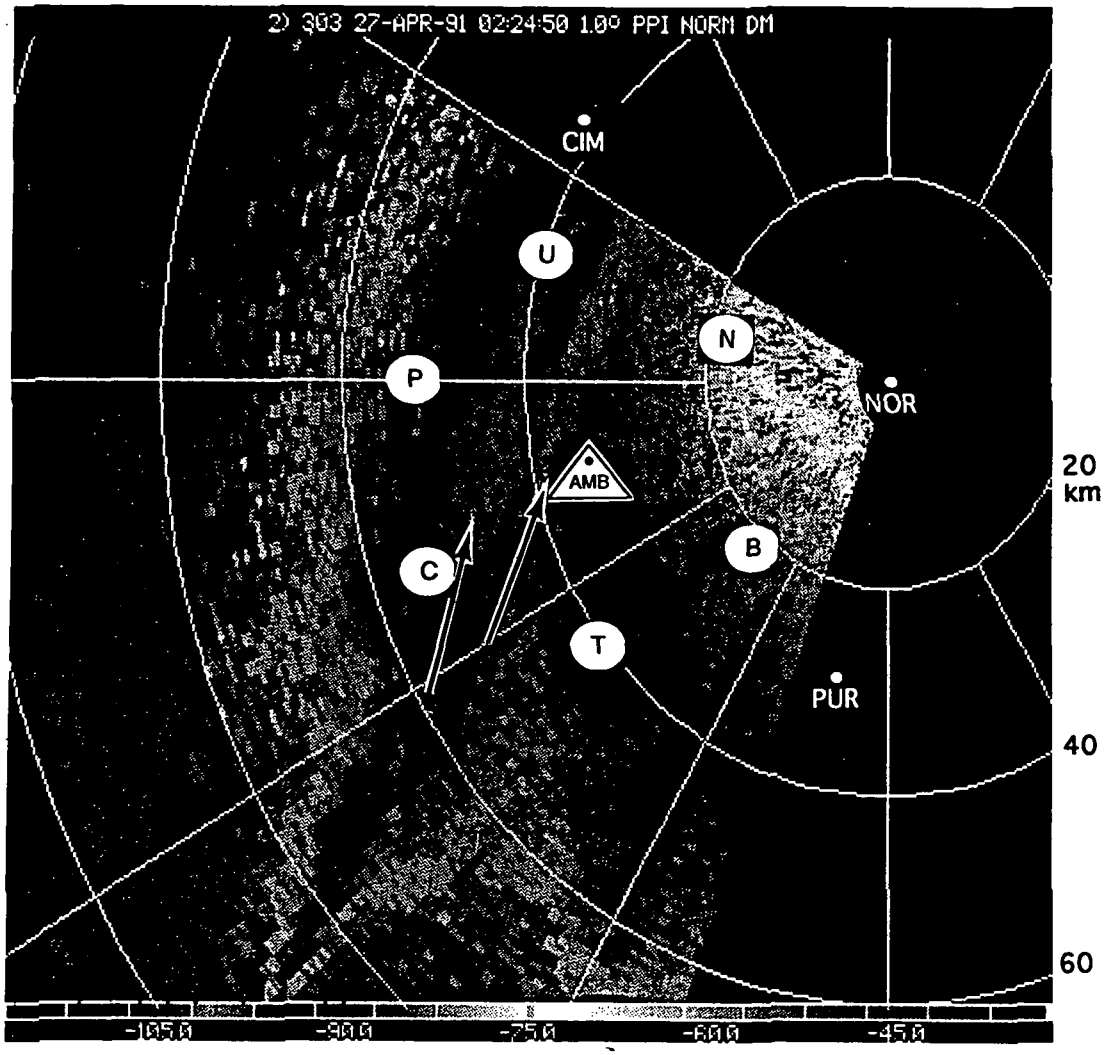

FIG. 15 Norman Doppler radar reflectivity (dBm) imagery (1.0° elevation angle) at 0225 UTC. Note double structured fine lines just west of Amber (AMB). The leading line is the bore, whereas the second fine line marks the location of the cold front with its density current microstructure. PAM stations,Cimarron (CIM) and Norman (NOR) radar sites, and the Purcell 405 MHz wind profiler (PUR) are also shown.

The bore was most easily identified as such in the PAM mesonet and microwave radiometer data at Amber. The bore is characterized by: (1) a 1.6 mb pressure jump, 1.3°C increase in temperature and sharp decrease in the moisture , and a sudden wind shift and gust in the PAM traces (Fig. 16), and by (2) a microscale spike in the liquid cloud water and a surrounding envelope of enhanced water vapor sensed by the microwave radiometer at Amber (Fig. 17). The surface warming is characteristic of bores, resulting from the downward mixing of potentially warmer air from above the surface-based inversion as the bore disrupts the stable layer by its passage (Koch et al. 1991). The wind shift and sudden drying can also be explained by this process, whereas the pressure rise is a hydrostatic reflection of the above-surface cooling accompanying the bore. The envelope of high water vapor content (horizontal scale of 13 km) apparently reflects the influence of the vertical circulation accompanying the bore, and the liquid water spike represents a roll-like "morning glory" cloud along the bore head (Smith 1988) that was evident by observers with the help of moonshine that evening. Notice that there are three separate small peaks in the precipitable water trace that correlate very well with similar features in the Amber surface pressure trace. It is believed that these are solitary waves located behind the bore head.

Also evident in these figures is the arrival of the cold front, which was felt in multiple pulses. For example, the temperature trace reveals the first temperature drop at 0252 UTC, followed by a more permanent drop at 0302. Likewise, the pressure and wind traces reveal two features, each of which appears approximately 5 min prior to those in the temperature trace. These two features are associated with the second fine line in the Norman radar display (Fig. 15). It is actually along this front that the severe convection erupts, rather than the bore front. Recent studies (e.g., Smith 1988; Koch et al. 1991) indicate that bores are frequently generated by the collapse of a density current into a surface-based stable layer and subsequently propagate away from the density current along the inversion waveguide. Thus, it is reasonable to hypothesize that the cold front was acting as a density current to trigger the formation of the bore. This matter is investigated further below.

The radar data were used to track the bore and density current features. The average velocity of the bore was determined to be C_b = 295°, 13.0 m s^{-1}, though it decelerated with time. The density current front travelled at a uniform speed of C_{dc} = 10.9 m s^{-1} throughout its lifetime. Bore-relative horizontal winds from the 915 MHz boundary layer profiler at Amber are shown in Fig. 18. Bore passage is evident at 0230 in these 5-min data (pulse width of 250 m). In fact, the updraft within the bore front of ~ 10 m s^{-1} (seen in the vertical beam data) was of such a small scale that it was impossible to subtract out its effects upon the off-beam data, resulting in loss of horizontal winds at the time of bore passage. A bore depth of h_b = 0.7 km is evident from the existence of positive front-relative flow of 10 m s^{-1}. Notice that a second region of even stronger positive flow develops after 0305 UTC in association with the passage of the cold front, which is similar to a density current.

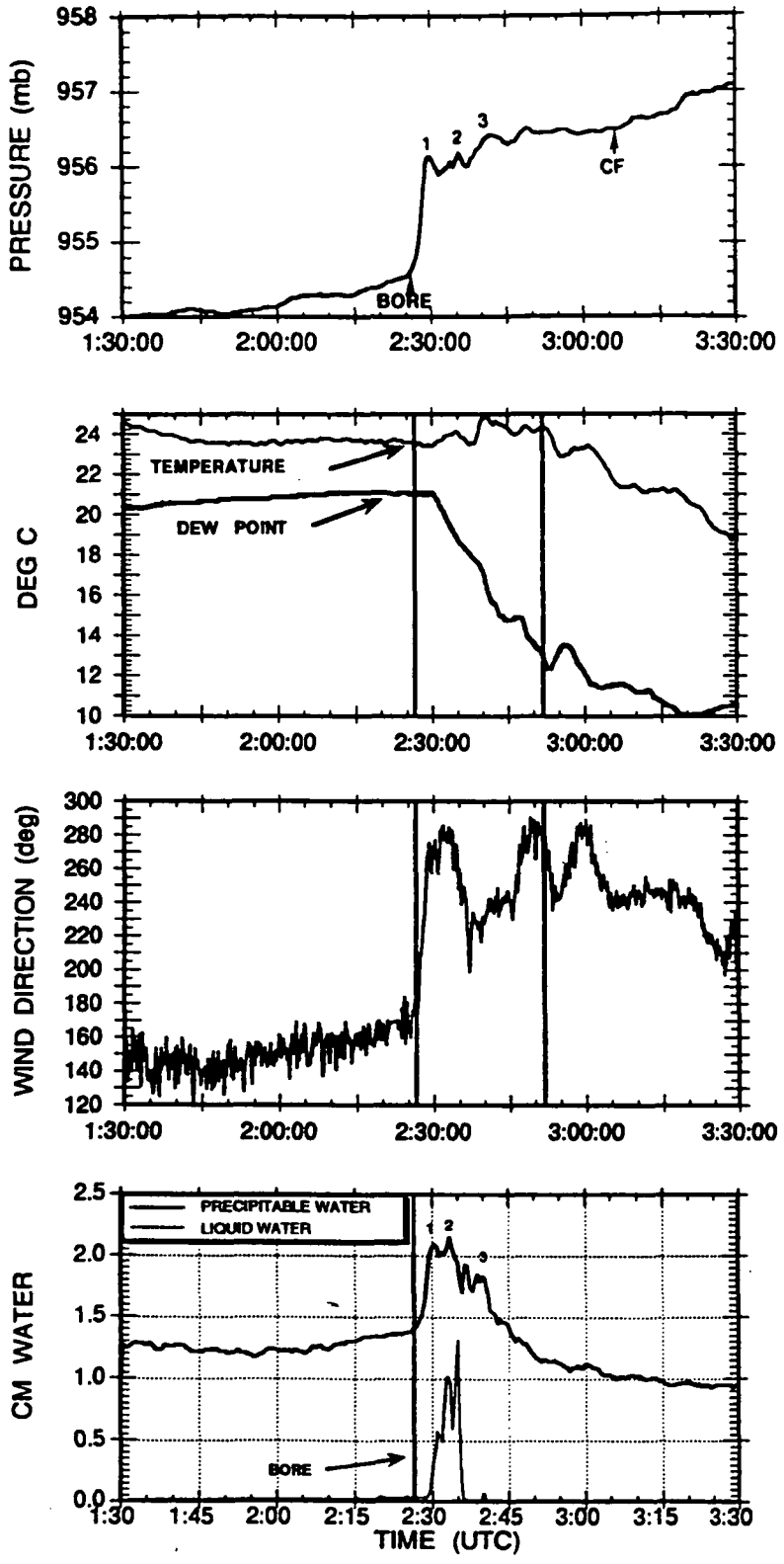

FIG. 16 Surface traces of pressure, temperature, dew point temperature, and wind direction from the 10 sec resolution data recorded at the Mobile CLASS system at Amber. Bore passage is at 0227 UTC, followed by several solitary waves and then the cold front (CF).

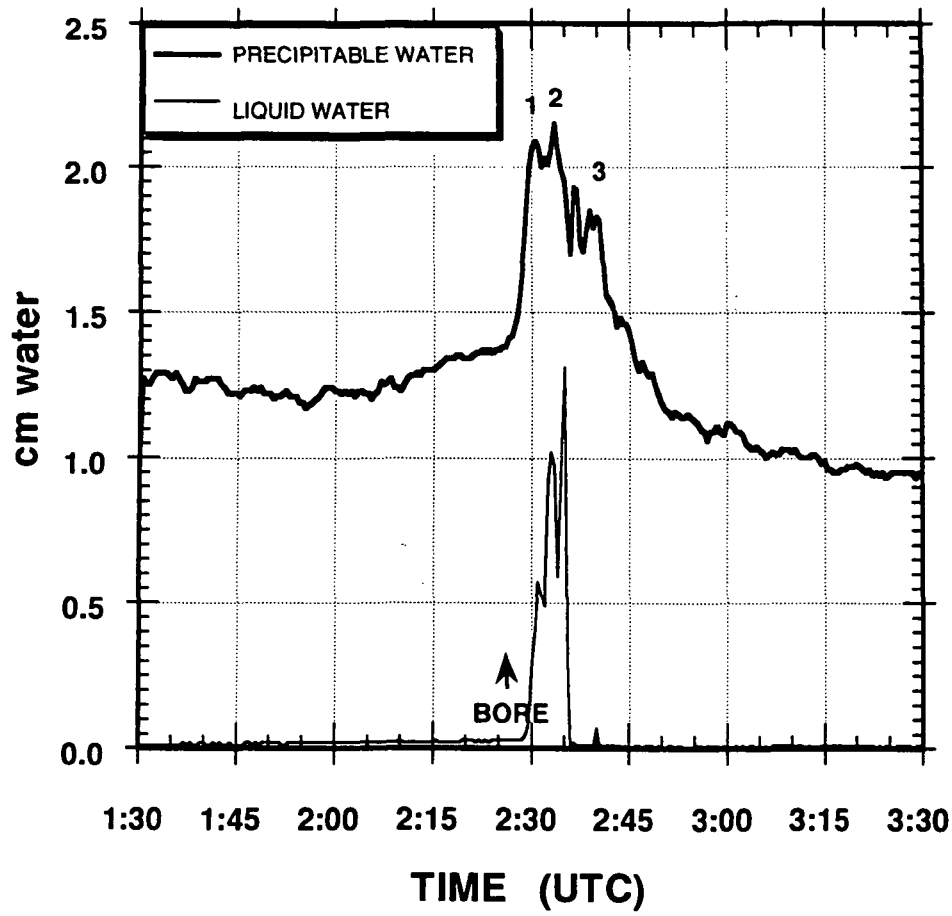

FIG. 17 Liquid and precipitable water traces from the microwave radiometer at Amber. Bore passage and solitary waves as given from Fig. 16 are shown.

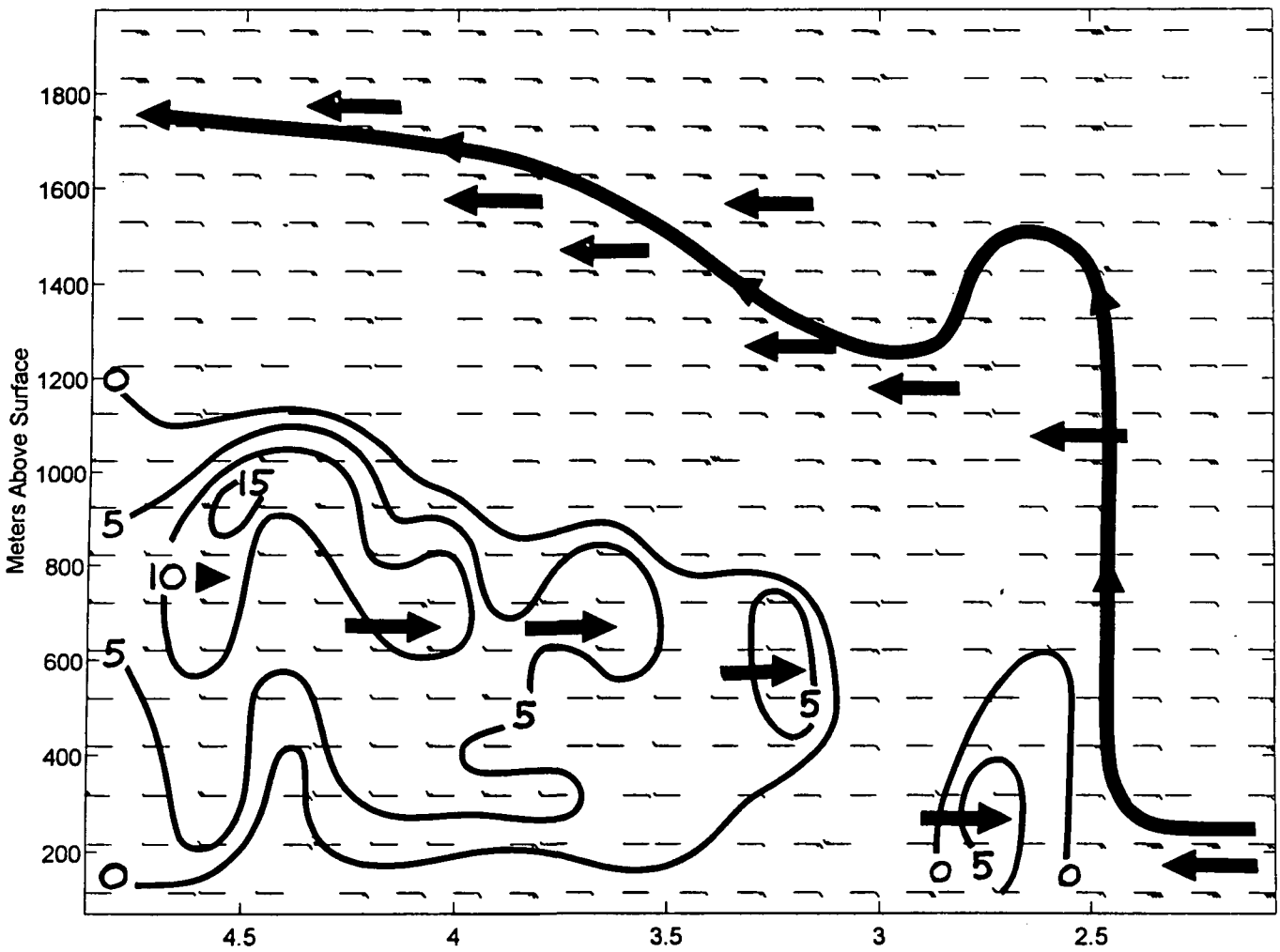

FIG. 18 Bore-relative winds ($U-C_b$) from 915 MHz wind profiler at Amber OK (UTC).

A strong surface-based inversion and low-level inflow relative to the bore were present ahead of the bore (0130 UTC sounding in Fig. 19). The other sounding displayed (0254 UTC) was taken 11 min before the cold front and 28 min after bore passage. Substantial cooling occurred following passage of the bore (and the solitary waves) over the lowest 2 km depth. The fact that this depth exceeds the 0.7 km depth seen in the profiler data indicates that isentropes above the bore were disturbed by its passage, similar to the findings of Koch et al. (1991). Notice also the region of positive bore-relative flow in the 0.3-0.7 km layer. This is seen to agree in height with the profiler display.

The stable layer ahead of the bore possessed a depth sufficient to support the formation of a bore presumably forced as the density current front intruded into this layer. This can be understood from application of two-layer hydraulic theory, according to which the type of disturbance so generated depends upon the Froude number (Fr) and the non-dimensional ratio do/ho, where do is the depth of the density current and ho is the inversion depth. The ratio of the density current speed to the phase speed of a long, internal gravity wave at the interface C_{dc}/C_{gw} determines Fr (details are provided in Koch et al. 1991). Use of C_{dc} = 10.9 m s^{-1}, h_o = 0.58 km, and $\Delta\theta$ = 4.05K (inversion strength from the CLASS data) gives Fr = 1.24. The value of d_o/h_o is more difficult to determine. We estimated the density current depth d_o from the average of the values: (a) obtained from classical density current theory using the observed pressure change at frontal passage (0.4 mb), and assuming that the cooling in the lowest 2 km of the sounding includes the density current effects, and (b) from the region of positive relative flow at 0310 UTC in the wind profiler display. Accordingly, we find that the depth ratio is d_o/h_o = 1.17. The combination of this parameter and the Froude number predicts an internal undular bore of strength h_b/h_o =2.1, from which we predict a bore depth of h_b =1.2 km. This value is in rather good agreement with the profiler observations (0.7 km). The bore speed can also be predicted from the theory using the bore strength value as a function of the gravity wave phase speed, from which we find C_b = 15.7 m s^{-1}, which agrees well with the observed value of 13.0 m s^{-1}.

This study has utilized a powerful combination of remote sensing systems to investigate the interactions between a cold front, a dryline, and the generation of both a density current and an undular bore. It has been shown that, although one could have easily inferred from the available surface data that a tornadic squall line was triggered as the front merged with the dryline, in fact convection was triggered along the front as it developed a density current-like leading edge. It appears that the bore was of insufficient depth, even though vertical velocities approached 10 m s^{-1}, to trigger the storms. Current research is aimed at attempting to understand why a density current developed along the front, and why the bore was not sufficient to trigger the deep convection.

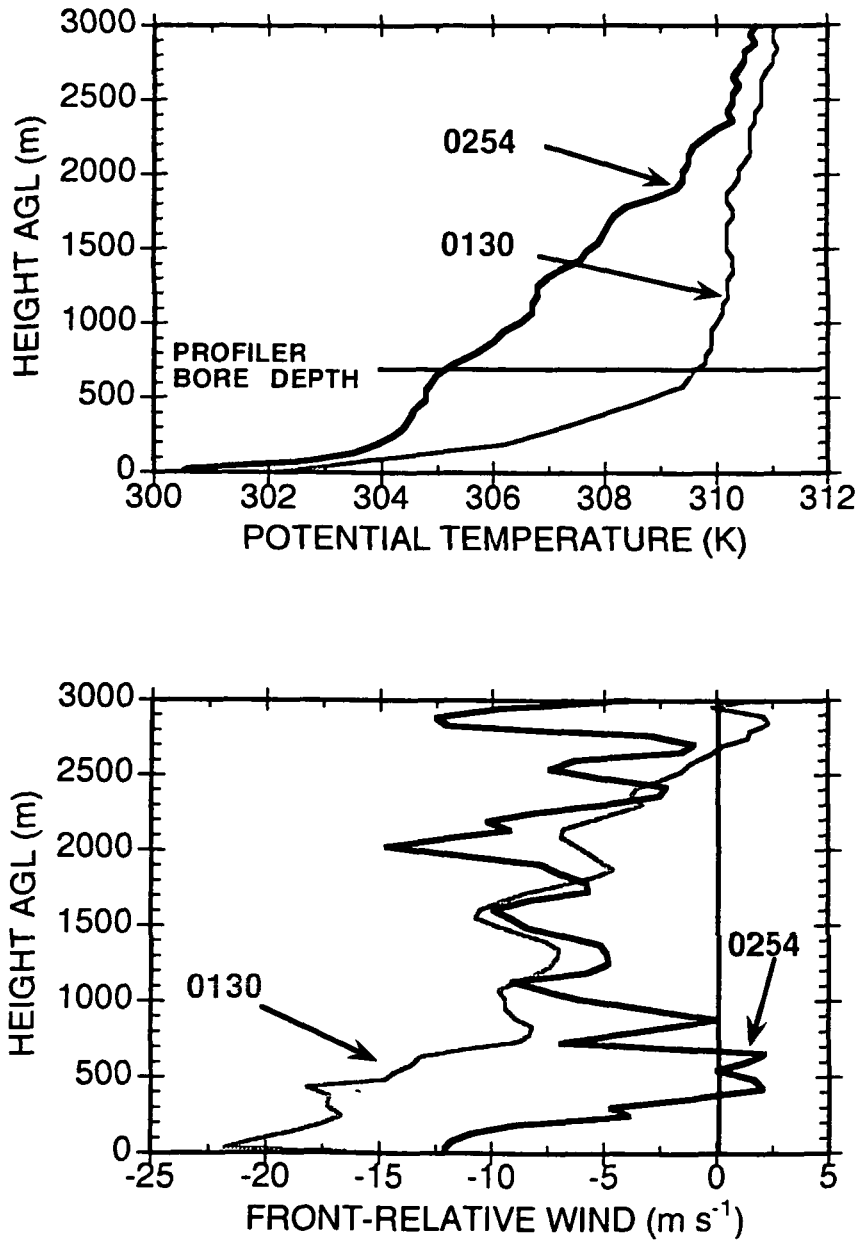

FIG. 19 Vertical profiles of potential temperature and bore front-relative winds determined from the Mobile CLASS sondes at 0130 UTC (pre-bore) and 0254 UTC (post bore/pre-cold front). Both soundings were taken within 13 km of Amber.

7. Publications and Presentations Resulting from this Grant

a. Refereed manuscripts appearing in scientific journals:

Koch, S. E., J. McQueen, and V. M. Karyampudi, 1995a: A numerical study of the effects of differential cloud cover on cold frontal structure and dynamics. *J. Atmos. Sci.* **52,** 937-964.

Koch, S. E., A. Aksakal, and J. T. McQueen, 1995b: The influence of mesoscale humidity and evapotranspiration fields on a model forecast of a cold frontal squall line. *Mon. Wea. Rev.* (cond. accept.).

Jin, Y., S. E. Koch, Y.-L. Lin, F. M. Ralph, and C. Chen, 1995: Numerical simulations of an observed gravity current and gravity waves in an environment characterized by complex stratification and shear. *J. Atmos. Sci.* (submitted).

b. Papers appearing in conference proceedings, preprints, and invited presentations:

Jin, Y., S. E. Koch, Y.-L. Lin, C. Chen, and F. M. Ralph, 1994: Numerical simulations of an observational case of density current and gravity waves. *Sixth Conference on Mesoscale Processes*, Portland, OR, Amer. Meteor. Soc., 164-167.

Koch, S. E., A. Aksakal, and J. T. McQueen, 1994: Boundary layer and frontal dynamical response to mesoscale detail in the initial state of water vapor and land surface fields. *10th Conference on Numerical Weather Prediction*, Portland, OR, Amer. Meteor. Soc., 438-440.

Koch, S. E., W. Clark, and E. Brandes, 1994: The forcing of deep convection by a density current-like cold front. *6th Conference on Mesoscale Processes,* Portland, OR, Amer. Meteor. Soc., 615-618.

Koch, S. E., J. T. McQueen, and V. M. Karyampudi, 1994: Unbalanced frontogenesis resulting from cloud-induced sensible heating effects. *6th Conference on Mesoscale Processes,* Portland, OR, Amer. Meteor. Soc., 395-398.

Koch, S. E., 1995: The dynamics of surface frontogenesis in the presence of sensible heating. Presented at NCAR, Boulder, CO.

8. References

Benard, P., J.-L. Redelsperger, and J.-P. Lafore, 1992: Nonhydrostatic simulation of frontogenesis in a moist atmosphere. Part I: General description and narrow rainbands. *J. Atmos. Sci.*, **49**, 2200-2217.

Berson, F. A., 1958: Some measurements of undercutting cold air. *Quart. J. Roy. Meteor. Soc.*, **84**, 1-16.

Blumen, W., 1980: A comparison between the Hoskins-Bretherton model of frontogenesis and the analysis of an intense surface frontal zone. *J. Atmos. Sci.*, **37**, 64-77.

Brundidge, K. C., 1965: The wind and temperature structure of nocturnal cold fronts in the first 1420 feet. *Mon. Wea. Rev.*, **93**, 587-603

Businger, S., W. H. Bauman III, and G. F. Watson, 1991: The development of the Piedmont front and associated outbreak of severe weather on 13 March 1986. *Mon. Wea. Rev.*, **119**, 2224-2251.

Carbone, R. E., 1982: A severe frontal rainband. Part 1: Stormwide hydrodynamic structure. *J. Atmos. Sci.*, **39**, 258-279.

Chang, J.-T., and P. J. Wetzel, 1991: Effects of spatial variations of soil moisture and vegetation on the evolution of a prestorm environment: a numerical case study. *Mon. Wea. Rev.*, **119**, 1368-1390.

Charba, J., 1974: Application of gravity current model to analysis of a squall-line gust front. *Mon. Wea. Rev.*, **102**, 140-156.

Chen, C., 1991: A nested-grid, non-hydrostatic, elastic model using a terrain-following coordinate transformation: The radiative-nesting boundary conditions. *Mon. Wea. Rev.*, **119**, 2852-2869.

Chen, C., and W. R. Cotton, 1983: A one-dimensional simulation of the stratocumulus-capped mixed layer. *Bound. Layer Meteorol.*, **25**, 289-321.

Chen, C., J. W. Rottman, and S. E. Koch, 1994: Numerical simulations of upstream blocking, columnar disturbances, and bores in stably stratified shear flows over an obstacle. *Mon. Wea. Rev.*, **122**, 2506-2529.

Crook, N. A., 1988: Trapping of low-level internal gravity waves. *J. Atmos. Sci.*, **45**, 1533-1541.

desBois, M., G. Seze, and G. Szejwach, 1982: Automatic classification of clouds on METEOSAT imagery: Application to high-level clouds. *J. Appl. Met.*, **21**, 401-412.

Dorian, P. B., S. E. Koch and W. C. Skillman, 1988: The relationship between satellite-inferred frontogenesis and squall line formation. *Wea. and Forecasting*, **3**, 319-342.

Doviak, R., and R. Ge, 1984: An atmospheric solitary gust observed with a Doppler radar, a tall tower and a surface network. *J. Atmos. Sci.*, **41**, 2559-2573.

Droegemeier, K. K., and R. B. Wilhelmson, 1985a: Three-dimensional numerical modeling of convection produced by interacting thunderstorm outflows. Part I: Control simulation and low-level moisture variations. *J. Atmos. Sci.*, **42**, 2381-2403.

—, and —, 1985b: Three-dimensional numerical modeling of convection produced by interacting thunderstorm outflows. Part II: Variations in vertical wind shear. *J. Atmos. Sci.*, **42**, 2404-2414.

Duynkerke, P. G., and A. G. M. Driedonks, 1987: A model for the turbulent structure of the stratocumulus-topped atmospheric boundary layer. *J. Atmos. Sci.*, **44**, 43-64.

Eady, E. T., 1949: Long waves and cyclone waves. *Tellus*, **1**, No. 3, 33-52.

Eliassen, A., 1962: On the vertical circulation in frontal zones. *Geofys. Publ.*, **24** (4), 147-160.

Fulton, R., D. S. Zrnic and R. J. Doviak, 1990: Initiation of a solitary wave family in the demise of a nocturnal thunderstorm density current. *J. Atmos. Sci.*, **47**, 319-337.

Garratt, J. R., 1988: Summertime cold fronts in Southeast Australia--behavior and low-level structure of main frontal types. *Mon. Wea. Rev.*, **116**, 636-649.

Garratt, J. R., and W. L. Physick, 1986: Numerical study of atmospheric gravity currents. Part I: Simulations and observations of cold fronts. *Beitr. Phys. Atmos.*, **59**, 282-300.

Goff, R. C., 1976: Vertical structure of thunderstorm outflows. *Mon. Wea. Rev.*, **104**, 1429-1440.

Haase, S. P., and R. K. Smith, 1989: The numerical simulation of atmospheric gravity currents. Part II: Environments with stable layers. *Geophys. Astrophys. Fluid Dyn.*, **46**, 35-51.

Hane, C. E., C. L. Ziegler, and H. B. Bluestein, 1993: Investigation of the dryline and convective storms initiated along the dryline: field experiments during COPS-91. *Bull. Amer. Meteor. Soc.*, **74**, 2133-2145.

Hoskins, B. J., 1971: Atmospheric frontogenesis: Some solutions. *Quart. J. Roy. Meteor. Soc.*, **97**, 139-153.

Hoskins, B. J., 1975: The geostrophic momentum approximation and the semi-geostrophic equations *J. Atmos. Sci.*, **32**, 233-242.

Hoskins, B. J., and F. P. Bretherton, 1972: Atmospheric frontogenesis models: Mathematical formulation and solution. *J. Atmos. Sci.*, **29**, 11-37.

Howells, P. A. C., and Y.-H. Kuo, 1988: A numerical study of the mesoscale environment of a southerly buster event. *Mon. Wea. Rev.*, **116**, 1771-1788.

Hsie, E.-Y., and R. A. Anthes, 1984: Simulation of frontogenesis in a moist atmosphere using alternative parameterizations of condensation and precipitation. *J. Atmos. Sci.*, **41**, 2701-2716.

Hsie, E.-Y., R. A. Anthes, and D. Keyser, 1984: Numerical simulation of frontogenesis in a moist atmosphere. *J. Atmos. Sci.*, **41**, 2581-2594.

Jin, Y., S. E. Koch, Y.-L. Lin, F. M. Ralph, and C. Chen, 1995: Numerical simulations of an observed gravity current and gravity waves in an environment characterized by complex stratification and shear. *J. Atmos. Sci.* (submitted).

Keyser, D., and R. A. Anthes, 1982: The influence of planetary boundary layer physics on frontal structure in the Hoskins-Bretherton horizontal shear model. *J. Atmos. Sci.*, **39,** 1783-1802.

Knight, D. J., and P. V. Hobbs, 1988: The mesoscale and microscale structure and organization of clouds and precipitation in midlatitude cyclones. Part XV: A numerical modeling study of frontogenesis and cold-frontal rainbands. *J. Atmos. Sci.*, **45,** 915-930.

Koch, S. E., 1984: The role of an apparent mesoscale frontogenetical circulation in squall line initiation. *Mon. Wea. Rev.*, **112,** 2090-2111.

Koch, S. E., and P. J. Kocin, 1991: Scale contraction processes leading to the formation of a severe frontal rainband. *Meteor. Atmosph. Phys.*, **46,** 123-154.

Koch, S. E., J. McQueen, and V. M. Karyampudi, 1995a: A numerical study of the effects of differential cloud cover on cold frontal structure and dynamics. *J. Atmos. Sci.* **52,** 937-964.

Koch, S. E., A. Aksakal, and J. T. McQueen, 1995b: The influence of mesoscale humidity and evapotranspiration fields on a model forecast of a cold frontal squall line. *Mon. Wea. Rev.* (cond. accept.).

Koch, S. E., W. Clark, and E. Brandes, 1994: The forcing of deep convection by a density current-like cold front. *6th Conference on Mesoscale Processes,* Portland, OR, Amer. Meteor. Soc., 615-618.

Koch, S. E., P. B. Dorian, R. Ferrare, S. H. Melfi, W. C. Skillman and D.Whiteman, 1991: Structure of an internal bore and dissipating gravity current as revealed by Raman lidar. *Mon. Wea. Rev.*, **119,** 857-887.

Lin, Y.-L., and H.-Y. Chun, 1991: Effects of diabatic cooling in a shear flow with a critical level. *J. Atmos. Sci.*, **48,** 2476-2491.

Marks, J. R., 1974: Acoustic radar investigations of boundary layer phenomena. NASA Tech. Report CR-2432, Marshall Space Flight Center, Huntsville, AL, 65 pp [NTIS N7423183].

Mellor, G. L., and T. Yamada, 1974: A hierarchy of turbulence closure models for planetary boundary layers. *J. Atmos. Sci.*, **31,** 1791-1806.

Miles, J. W., 1961: On the stability of heterogeneous shear flows. *J. Fluid Mech.*, **10,** 496-508.

Moncrieff, M. W., 1989: Analytical models of narrow cold-frontal rainbands and related phenomena. J. *Atmos. Sci.*, **46,** 150-162.

Parsons, D. B., C. G. Mohr, and T. Gal-Chen, 1987: A severe frontal rainband. Part III: Derived thermodynamic structure. *J. Atmos. Sci.*, **44,** 1613-1631.

Pinkerton, J. E., 1978: Numerical experiments on boundary layer effects on frontal structure. Ph.D. dissertation [available from University Microfilms International, Ann Arbor, Michigan, U. S. A.], 213 pp.

Proctor, F. H., 1987a: The terminal area simulation system. Volume I: theoretical formulation. NASA Contractor Report 4046, NASA, Washington, DC, 176 pp.

Proctor, F. H., 1987b: The terminal area simulation system. Volume II: verification experiments. NASA Contractor Report 4047, NASA, Washington, DC, 112 pp.

Ralph, F. M., C. Mazaudier, M. Crochet, and S. V. Venkateswaran, 1993: Doppler sodar and radar wind-profiler observations of gravity-wave activity associated with a gravity current. *Mon. Wea. Rev.*, **121**, 444-463.

Raymond, D. J., and R. Rotunno, 1989: Response of a stably stratified flow to cooling. *J. Atmos. Sci.*, **46**, 2830-2837.

Reeder, M. J., 1986: The interaction of a surface cold front with a prefrontal thermodynamically well-mixed boundary layer. *Aust. Met. Mag.*, **34**, 137-148.

Reeder, M. J., and R. K. Smith, 1987: A study of frontal dynamics with application to the Australian summertime "cool change". *J. Atmos. Sci.*, **44**, 687-705.

Rottman, J. W., and J. E. Simpson, 1989: The formation of internal bores in the atmosphere: A laboratory model. *Quart. J. Roy. Meteor. Soc.*, **115**, 941-963.

Sawyer, J. S., 1956: The vertical circulation at meteorological fronts and its relation to frontogenesis. *Proc. R. Soc. London*, **A234**, 346-362.

Scorer, R. S., 1949: Theory of waves in the lee of mountains. *Quart. J. Roy. Meteor. Soc.*, **75**, 41-56.

Segal, M., F. W. Purdom, J. L. Song, R. A. Pielke, and Y. Mahrer, 1986: Evaluation of cloud shading effects on the generation and modification of mesoscale circulations. *Mon. Wea. Rev.*, **114**, 1201-1212.

Segal, M., W. L. Physick, J. E. Heim, and R. W. Arritt, 1993: The enhancement of cold-front temperature contrast by differential cloud cover. *Mon. Wea. Rev.*, **121**, 867-873.

Shapiro, M. A., 1984: Meteorological tower measurements of a surface cold front. *Mon. Wea. Rev.*, **112**, 1634-1639.

Shapiro, M. A., T. Hampel, D. Rotzoll and F. Mosher, 1985: The frontal hydraulic head: A micro-α scale (~1 km) triggering mechanism for mesoconvective weather systems. *Mon. Wea. Rev.*, **113**, 1166-1183.

Simpson, J. E., 1987: *Gravity Currents: in the Environment and the Laboratory.* Wiley & Sons, 244 pp.

Smith, R. K., 1988: Travelling waves and bores in the lower atmosphere: The 'Morning Glory' and related phenomena. *Earth-Science Reviews*, **25**, Elsevier Science, 267-290.

Smith, R. K., and M. J. Reeder, 1988: On the movement and low-level structure of cold fronts. *Mon. Wea. Rev.*, **116**, 1927-1944.

Sun, W.-Y., and Y. Ogura, 1979: Boundary-layer forcing as a possible trigger to a squall-line formation. *J. Atmos. Sci.*, **36**, 235-254.

Thompson, W. T., and S. D. Burk, 1991: An investigation of an arctic front with a vertically nested mesoscale model. *Mon. Wea. Rev.*, **119**, 233-261.

Wakimoto, R. M., 1982: The life cycle of thunderstorm gust fronts as viewed with Doppler radar and rawinsonde data. *Mon. Wea. Rev.*, **110**, 1060-1082.

Williams, R. T., 1974: Numerical simulation of steady-state fronts. *J. Atmos. Sci.*, **31**, 1286-1296.

Young, G. S., and R. H. Johnson. 1984: Meso- and microscale features of a Colorado cold front. *J. Climate and Appl. Meteor.*, **23**, 1315-1325.